

Key Points:

- Secondary cratering dominates impact gardening in the top few meters
- Water ice on the Moon may be billions of years old
- Water ice on Mercury is no more than 200 million years old

Correspondence to:

E. S. Costello,
ecostello@higp.hawaii.edu

Citation:

Costello, E. S., Ghent, R. R., Hirabayashi, M., & Lucey, P. G. (2020). Impact gardening as a constraint on the age, source, and evolution of ice on Mercury and the Moon. *Journal of Geophysical Research: Planets*, 125, e2019JE006172. <https://doi.org/10.1029/2019JE006172>

Received 14 AUG 2019

Accepted 20 JAN 2020

Accepted article online 7 FEB 2020

Impact Gardening as a Constraint on the Age, Source, and Evolution of Ice on Mercury and the Moon

E. S. Costello^{1,2} , R. R. Ghent³ , M. Hirabayashi⁴ , and P. G. Lucey²

¹Department of Earth Science, University of Hawaii at Manoa, Honolulu, HI, USA, ²Hawaii Institute of Geophysics and Planetology, Honolulu, HI, USA, ³Planetary Science Institute, Tucson, AZ, USA, ⁴Department of Aerospace Engineering, Auburn University, Auburn, AL, USA

Abstract We update an analytic impact gardening model (Costello et al., 2018, <https://doi.org/10.1016/j.icarus.2018.05.023>) to calculate the depth gardened by impactors on the Moon and Mercury and assess the implications of our results for the age, extent, and source of water ice deposits on both planetary bodies. We show that if the water presently on the Moon has a primordial origin, it may have been 4–15 m thick. If ice deposits are buried, they may be as shallow as 3 cm or as deep as 10 m and provide a gradient of probability for ice gardened into a column. Our calculations for gardening on Mercury show that thermal lag deposits will be reworked into the background over 200 Myr, and, thus, the most recent large-scale deposition of ice on Mercury must have occurred no more than 200 Myr ago. We also find that gardening mixes incremental layers of ice with underlying regolith and prevents the growth of pure ice deposits by continuous supply. We conclude that ice deposits on the Moon and Mercury are likely the result of sudden and voluminous deposition.

Plain Language Summary The Moon and Mercury have water ice in permanently shadowed regions at their poles; however, while Mercury's poles are rich in water ice, the Moon's are relatively sparse. Impact cratering mixes surface material, bringing buried ice upward to a relatively hostile surface in a process called “impact gardening.” We apply a revised impact gardening model to investigate the depth from which ice is mixed upward by impacts as a function of time and discover the following: (1) Ice on the Moon may have been mixed with underlying regolith or buried under many meters of dry regolith; (2) the most recent large-scale delivery of water to Mercury happened no more than 200 Myr ago; (3) what ice exists at the poles of the Moon and Mercury was probably delivered suddenly and voluminously; and (4) the differences between the abundance of water ice on the Moon and Mercury will only become more pronounced with time as impact gardening destroys surface ice on the Moon and only scratches the surface of Mercury's extensive deposits.

1. Introduction

The poles of the Moon and Mercury both have locations permanently shielded by topography from sunlight inside of which temperatures are low enough to allow the presence of water ice that can persist for billions of years against sublimation. The similarity ends there. The poles of Mercury are unambiguously ice-rich, while the poles of the Moon are largely dry. Earth-based radar observations revealed charismatic radar-bright regions in permanently shadowed regions (PSRs) near Mercury's north and south poles that showed reflectivity and polarization properties that were more like the icy objects of the outer solar system than the rocky Moon or the rest of Mercury (Harcke, 2005; Harmon & Slade, 1992; Harmon et al., 1994; Slade et al., 1992). In 2011 NASA's MERcury Surface, Space ENvironment, GEochemistry, and Ranging (MESSENGER) mission entered orbit around Mercury and explored the composition of the radar-bright regions. MESSENGER neutron spectra showed elevated hydrogen at Mercury's north pole, and Lawrence et al. (2013) concluded that the radar-bright regions were deposits of nearly pure water ice. On Mercury, every surface and shallow subsurface location that is cold enough to preserve water ice from sublimation shows radar backscatter enhancements (Chabot et al., 2013; Paige et al., 2013; Vasavada et al., 1999), and deposits are thought to be up to 30 m thick (Deutsch et al., 2018; Eke et al., 2017; Susorney et al., 2019).

In contrast, the search for ice on the Moon is ongoing, and results have been comparatively dry, showing that the Moon is relatively ice-free compared to Mercury. It has long been postulated that lunar PSRs could

hold water ice (Urey, 1952; Watson et al., 1962). Neutron spectroscopy observations from both the Lunar Prospector Neutron Spectrometer and the Lunar Exploration Neutron Detector instrument on board the Lunar Reconnaissance Orbiter (LRO) have shown elevated hydrogen at the poles to their sensing depth of about a meter; however, neutron spectroscopy is sensitive only to the presence of hydrogen, not its molecular bonds (e.g., Boynton et al., 2012; Feldman et al., 2000; Miller, 2012). It is unknown if the H anomalies are a signature of molecular water. Strong evidence for the presence of water ice in the subsurface came from the Lunar Crater Observation and Sensing Satellite mission, which upon crashing into a PSR inside the south polar crater, Cabeus, produced a volatile-rich plume, and data showed that the regolith at Cabeus may have a water concentration of $\sim 5\%$ by mass (Colaprete et al., 2010). Earth-based and orbital radar observations of the lunar poles have shown indications for circular polarization ratio anomalies inside PSRs that could indicate buried ice, but these experiments conclusively show that extensive ice deposits like those seen on Mercury are not present on the Moon (Campbell et al., 2006; Fa & Cai, 2013; Neish et al., 2011; Nozette et al., 2001; Spudis et al., 2013; Stacy et al., 1997; Thomson et al., 2012). At the surface, evidence of patchy surface water that covers roughly 10% of the total PSR area has been presented by workers using LRO Lunar Orbiter Laser Altimeter reflectance measurements, LRO Lyman Alpha Mapping Project UV spectra, and Chandrayan Moon Mineral Mapper infrared spectra, coupled with temperature data from the LRO Diviner thermal radiometer (e.g., Fisher et al., 2017; Hayne et al., 2015; Li et al., 2018; Milliken & Li, 2017; Zuber et al., 2012). A statistical approach by Rubanenko et al. (2019) concluded that craters in the south lunar polar region have relatively low depth-diameter ratios and suggested that the shallowing is caused by buried ice; however, because of the statistical nature of the work, they could not identify individual shallowed candidate craters, and the mystery of why there might be an asymmetric distribution of water by any source between the north and south poles remains a mystery and concern. While the Moon's poles are not completely dry, the limited distribution and quantity of water ice are in stark contrast with Mercury's extensive icy deposits.

The differences in the water concentrations at the poles of the Moon and Mercury may be explained by luck or age. The Moon's ice may be the ancient relic of Mercury-like ice deposits formed by volcanic outgassing or cometary impacts (Needham & Kring, 2017; Siegler et al., 2016) or simply the steady accumulation of water formed from solar wind-implanted hydrogen (Crider & Vondrak, 2000, 2002; Hurley & Benna, 2018; Liu et al., 2012).

In contrast, Mercury may have gotten lucky recently—struck by a statistically anomalous comet or water-bearing asteroid no more than 300 Myr ago that left Mercury's surface scarred by the crater Hokusai and its poles full of water ice (Ernst et al., 2018). In addition to age or luck, Mercury's ice evolves over time differently from the Moon's. Marchi et al. (2005) showed that the flux of 1 cm to 100 m diameter meteorites is about an order of magnitude lower at Mercury than at the Moon. These impactors and the secondary craters that they generate are the dominant impact gardeners of the top few meters of material on the Moon and Mercury. A possible scenario is that the Moon once had Mercury-like ice deposits that have been pulverized, exposed to significant loss, and mixed with underlying regolith by a more intense meter-scale impact environment.

Impacts continue to shape the surfaces of the Moon and Mercury. The effects of impact gardening on the regolith of both bodies have been studied since the Apollo era (e.g., Cintala, 1992; Costello et al., 2018; Gault et al., 1974). What affects the regolith must also affect polar ice deposits. In the present study we update and extend our impact gardening model (Costello et al., 2018) that calculates the depth excavated and overturned by impacts as a function of time to investigate the effects of impact gardening on ice at the poles of the Moon and Mercury. Our model is validated by the lunar case and includes a treatment of secondary impacts, which are critically important for understanding regolith overturn from the surface to meter scale depths (McEwen & Bierhaus, 2006; McEwen et al., 2005; Costello et al., 2018; Speyerer et al., 2016). We compare our impact gardening model predictions to observations of the distribution of ice and ice-related features on both planets to constrain their age, source, and evolution over time.

2. Gardening Model: Updates to the Treatment of Cumulative Craters

Costello et al. (2018) presented an analytical model that describes the frequency with which a point at depth is included in the excavated volume of a crater with some probability by modeling cratering as a marked homogeneous Poisson process, which were first applied to the problem of impact gardening by Gault et al. (1974). In this paper, we update the marked homogeneous Poisson process model by Costello et al. (2018)

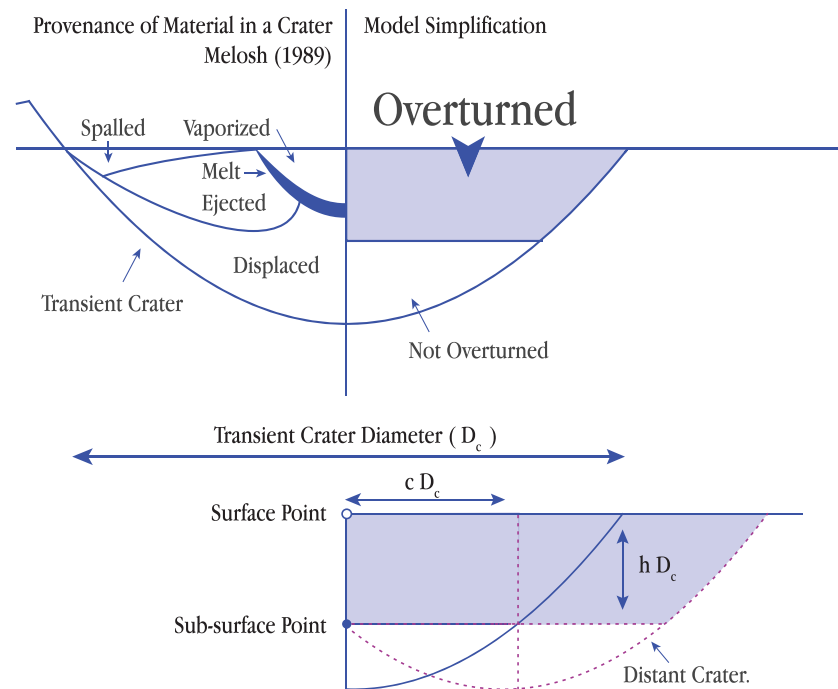


Figure 1. The geometry of the model following Figure 2 of Costello et al. (2018). The scaling value h is the fraction of the crater diameter, D_c , that has been excavated by a cratering event. The scaling value c is controlled by the shape of the crater bowl and describes the distance at which a crater must strike (in terms of crater diameter) in order to overturn a point at depth.

by revising a flaw in the treatment of the cumulative impactor distribution, which results in a more accurate prediction of impact overturn (the process by which impacts mechanically churn the regolith) driven by small crater sizes. Here, we detail the differences between the current treatment and that of Costello et al. (2018) and discuss the implications for the predictions of each treatment. We begin by following equation (23) of Costello et al. (2018), which was constructed using a geometric argument such that when a reference area is large, the average number of cratering events can be approximated as the following equation:

$$\lambda = N\pi \frac{(cD)^2}{4} t \quad (1)$$

where N is the total number of craters emplaced of constant diameter D that form per area and time, t is time, and c is a scaling factor for a new crater of D to disturb a point along the center point of an existing crater of diameter D_c at depth hD (Figure 1). The average number of events, λ , is unitless. Values for λ come from solutions to the cumulative Poisson probability equation:

$$P = 1 - \sum_{n=0}^{\infty} \frac{e^{-\lambda} \lambda^n}{n!} \quad (2)$$

for combinations of λ and the cumulative number of times, n , newly emplaced craters disturb at a given area over time. The values for λ used in this work can be found in Table 1 of Costello et al. (2018). Equation (1) is the same expression derived and used in Costello et al. (2018).

Here, we revise our model to correctly treat the effects of craters larger than a reference diameter D_c , which also influence our reference point (Figure 2). Costello et al. (2018) solved equation (1) for N , the total number of craters per area per unit time, and integrated over diameter D to capture the effects of craters larger than reference diameter D_c . This leads to an expression with units of craters per length, rather than area, per time. Here, instead, we express equation (1) in discrete form as

$$\lambda = tc^2 \left(\Delta N_1 \frac{\pi D_1^2}{4} + \Delta N_2 \frac{\pi D_2^2}{4} + \dots + \Delta N_{MAX} \frac{\pi D_{MAX}^2}{4} \right) \quad (3)$$

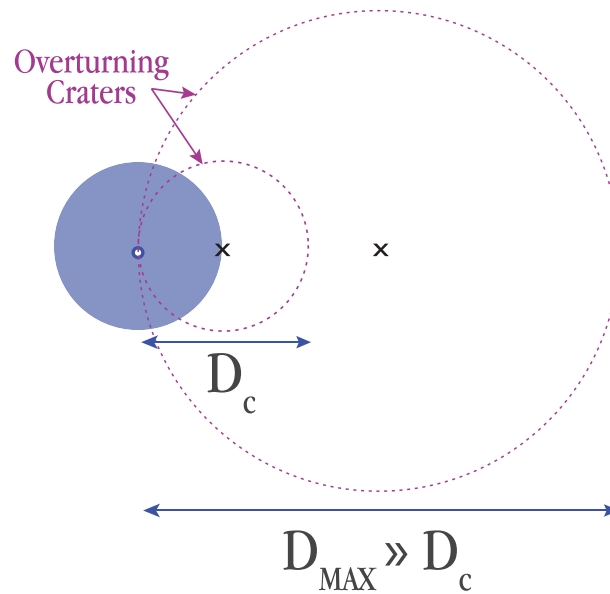


Figure 2. Craters that are larger than diameter D also affect a surface point following Figure 3 of Costello et al. (2018).

where ΔN_i is the number of emplaced craters with a diameter $D_i (\geq D_c)$ per area per time, i is an index up to the number MAX , and cD_c is the distance at which a crater must strike in order to overturn a point at depth (Figure 1). The sum of ΔN_i over different crater sizes is equal to the total number of emplaced craters at all sizes. This expression recognizes that the distribution of craters varies as a function of crater size (e.g., Hirabayashi et al., 2018), and the sum gives the total number of emplaced craters at all sizes. We then write equation (3) in continuous form:

$$\lambda = \left| tc^2 \int_{D_c}^{D_{MAX}} \frac{\pi D^2}{4} \frac{dN_c}{dD} dD \right| \quad (4)$$

where N_c is the cumulative crater production function (CPF) and has units of number per unit area and time. The average number of events per interval, λ , is an inherently positive interval scale quantity and the direction of our integration does not matter. Whether we begin counting large craters and finish counting small or begin small and finish large, the cumulative number of craters will be equal; to capture the inherent positivity of number-space, we include absolute values around the right-hand side of the equation. We include absolute values and adhere to the classical calculus understanding of equation (4), deviating from the standard assumption that a cumulative crater distribution is always positive (Appendix I of Crater Analysis Techniques Working Group, 1979) such that the model is prepared to explore distributions that change with crater size, should future workers wish to subdivide it.

The effect of the Costello et al. (2018) treatment is an overprediction of the depth overturned by impacts for very young ages and small crater sizes (due to the incorrect exponent of the N vs. t curve). The cumulative number of small craters are more likely to be affected by a wider range of craters; thus, the Costello et al. (2018) results for shallow gardening are effected by the error. In contrast, the predicted overturn depths for older ages and large crater sizes were generally unaffected (Figure 3). However, the uncertainty associated with the slope of the CPF is large for small craters; consequently, the Costello et al. (2018) model gave generally consistent results with empirical data. The remainder of the Costello et al. (2018) mathematical treatment, and the main result outlined in the paper—the idea that the gardening effects of secondary impacts are necessary to describe observations of reworking on the Moon—stand as published.

CPFs represent the number of craters of a given diameter that form on an area per unit time (e.g., Crater Analysis Techniques Working Group, 1979; Ivanov et al., 2001, 2002; Neukum, 1983). We use CPFs in their cumulative form, which give the number of craters of diameter D and larger that form on an area per unit time (Crater Analysis Techniques Working Group, 1979). Let us assume that craters produced on planetary bodies follow a cumulative power law size frequency distribution:

$$N_c = uD^v \quad (5)$$

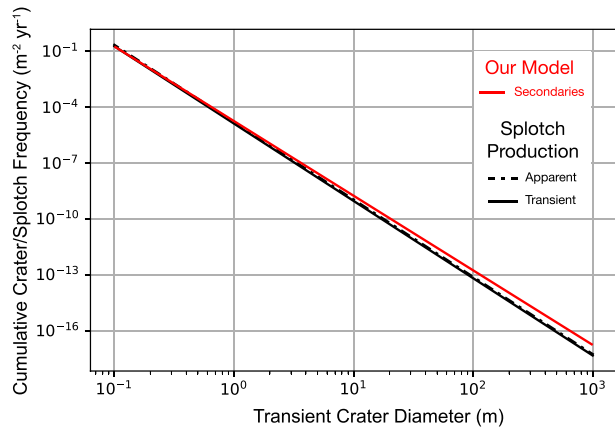


Figure 3. We plot the cumulative frequency of our modeled secondaries following the method of Costello et al. (2018) and assuming craters are in the strength regime and forming in regolith and compare to the production of spotched reported by Speyerer et al. (2016). The scaling from apparent to transient diameter changes very little, and the functions fit well.

where u and v are the parameters that control the shape of the CPF. The shape parameter u is always positive and has units of craters per $[L]^{2+v}$ and time. The shape parameter v is a dimensionless power index and is usually negative; that is, there are usually more small craters than large craters. We solve for λ by substituting equation (5) into equation (4):

$$\lambda = \left| \frac{\pi t c^2}{4} \frac{uv}{v+2} [D_c^{v+2} - D_{MAX}^{v+2}] \right| \quad (6)$$

D_{MAX} is defined as a crater size much larger than the minimum crater diameter (D_c) required to overturn to a certain depth (Figure 2) and may be the maximum crater diameter observed on a considered planetary body. When $v < -2$ (a common crater frequency power index is ~ -3), as $D_{MAX} \rightarrow \infty$ the D_{MAX} term in equation (6) goes to 0, and the expression is simplified. We solve equation (6) for D_c :

$$D_c = \left| \left[\left(\frac{v+2}{vu} \right) \left(\frac{4\lambda}{\pi t c^2} \right) \right]^{\frac{1}{v+2}} \right| \quad (7)$$

and the resulting equation (7) gives the frequency a surface point is interacted with craters D_c and larger following a Poisson distribution and

where, at the surface, $c = 1$. When we calculate overturn depth, $c < 1$ because craters must strike closer to a given point to excavate a point a depth (see Figure 1).

We define the depth of overturn (Λ) as a fraction of crater diameter (Figure 1):

$$\Lambda = h D_c \quad (8)$$

where h is the dimensionless excavation depth-fraction of crater diameter. Substituting equation (7) into equation (8), we arrive at the final form of the analytic model for the depth of impact gardening:

$$\Lambda = \left| h \left[\left(\frac{v+2}{vu} \right) \left(\frac{4\lambda}{\pi t c^2} \right) \right]^{\frac{1}{v+2}} \right| \quad (9)$$

where Λ is the depth of overturn as a function of time. This simple analytical function takes in the parameters for a cumulative power law flux, ($N_c = u D^v$) and a cumulative Poisson distribution-derived average number of events (λ) and gives us the minimum frequency with which a point at the depth Λ is in the excavated volume of a crater. We can read equation (9) as follows: Material at Λ depths has been brought to the surface by impacts that have occurred at least n times given the value for λ determined by a given probability, which is available in Table 1 of Costello et al. (2018). In its simplest form, the overturn function follows a power law function of time:

$$\Lambda = A t^{-B} \quad (10)$$

where

$$A = \left| h \left[\left(\frac{v+2}{vu} \right) \left(\frac{4\lambda}{c^2 \pi} \right) \right]^{\frac{1}{v+2}} \right| \quad (11)$$

and

$$B = \frac{1}{v+2} \quad (12)$$

The power index of the reworking depth (B) must be negative and v must be < -2 for the model to describe physical reality—small, shallowly overturning impacts are more likely than large, deeply overturning impacts. Fortunately, most predictions of CPFs for secondary craters, which dominate the mechanical churning of the uppermost meter or so, have relatively steep power indices (~ -4 ; e.g., Bierhaus et al., 2005; McEwen et al., 2005; Speyerer et al., 2016), satisfying the requirement that v be < -2 .

Costello et al. (2018) modeled a CPF from a power law impact flux and scaling laws for the size of a crater given impactor momentum and the material properties of the target. Equations (38) and (42) in Costello et al.

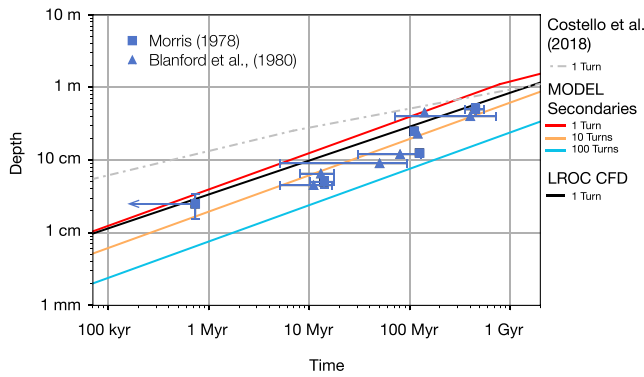


Figure 4. All overturn contours plotted here represent the deepest depth overturned at least one time over the time interval on the x axis with 99% probability. The model results using the size frequency distribution of small albedo anomalies observed in LROC temporal pairs (Speyerer et al., 2016) (solid black line) fits exceedingly well against the reworking of surface-correlated space weathering products in the top meter of regolith calculated from Apollo cores by Morris (1978) and Blanford (1980) and our model results using assumptions about the production of secondary impacts. The model results using a secondary impact flux derived from the Brown et al. (2002) flux of primary impacts fits both the LROC reworking rate and the reworking observed in Apollo cores. Compared to the results of Costello et al. (2018) (gray dot-dashed line plotted following the results shown in Figure 4 of Costello et al., 2018), the updates to the model decrease the rate of overturn at small scales by changing the magnitude and power law slope of the overturn function.

(2018) describe the production function from the impact flux and the scaling to crater size using the scaling laws presented in Holsapple (1993). The lithostatic pressure at a depth equivalent to the projectile radius, which must be overcome for excavation to occur, is $\rho g R_m$, where R_m is the impactor radius, g is gravity, and ρ is the density of the target. For small impactors, the effective target yield strength is greater than $\rho g R_m$, and the scaling from impactor size to crater size is in the strength regime. For large impactors, the gravity term is much greater than the target yield strength and the scaling from impactor size to crater size is in the gravity regime. The shape parameters u and v for the CPF can be calculated for impacts in the strength and gravity regime in terms of impact flux, Holsapple (1993) scaling from impactor size to crater size, and the Poisson expression as follows per Costello et al. (2018) equations (33)–(45):

$$u = \begin{cases} \sin(\theta)^{\frac{2}{3}} & a \left[\frac{1}{\delta(\gamma\alpha^\beta)^{1/3}} \right]^b & \text{in Strength Regime} \\ \sin(\theta)^{\frac{1}{3}} & a \left[\frac{1}{\delta(\gamma\epsilon^\beta)^{1/3}} \right]^{\frac{3b}{3+\beta}} & \text{in Gravity Regime} \end{cases} \quad (13)$$

where $\alpha = K_2 \left(\frac{Y}{\rho_t v_f^2} \right)^{\frac{2+\mu}{2}}$, $\beta = \frac{-3\mu}{2+\mu}$, $\delta = 2K_r$, $\gamma = \frac{K_1 \pi \rho_m}{6\rho_t}$, $\epsilon = \left(\frac{g}{2v_f^2} \right) \left(\frac{\rho_m}{\rho_t} \right)^{\frac{1}{3}}$, following Costello et al. (2018), and where K_r , K_d , K_1 , and K_2 are empirically derived scalars that depend on the target material (and where K_2 is more typically defined inside a power of $(2 + \mu)/2$; e.g., Holsapple, 1993), ρ_m is the density of the impactor, ρ_t is the target bulk density, g is the gravity of the target object, Y is the target yield strength, μ is an empirically derived scalar that depends on the target porosity, and v_f is the final velocity of the object upon impact. A method to calculate the strength-gravity transition depth can be found in Costello et al. (2018). When we plot overturn as a function of time we will see a kink at the strength-gravity transition where the overturn function changes slope and magnitude following equation (13) (see Figures 3 or 4). Although esthetically messy with abundant parameters, our model offers control of these input parameters and allows the comparison of predicted reworking depths in targets that are rocky or icy.

Estimates of production functions from crater counts risk errors at small scales from resolution limits, human error, contamination by secondary impacts, and erasure if craters are in equilibrium (e.g., Minton et al., 2019). When craters are in equilibrium “craters of the given size are being produced at the same rate at which they are being destroyed” (Gault, 1970). It is impossible to calculate the number of craters that form on a surface over a time interval if those craters are in equilibrium using observations of the surface alone. Our method of using a size-frequency distribution of impacting bodies (e.g., the bolide flux presented by Brown et al., 2002, which is valid down to meteorite sizes of ~ 1 cm) and the scaling from impactor size to crater size provides a way to “see through” crater equilibrium.

We update the depth fraction of crater diameter that is overturned (h) to capture the relatively shallow depth-diameter of low energy secondary craters ($d/D \approx 0.2$, where d is the final crater depth; e.g., Bierhaus, et al., 2010; McEwen et al., 2005; Melosh, 1989) and assume that only the top half of a crater is excavated such that: $h = 0.02 \times 0.5 = 0.04$ (assuming only half of a crater depth is overturned following Speyerer et al., 2016). We also inherit the scaling parameter c from Costello et al. (2018), which describes the distance craters must form along the center point of an existing crater of diameter D at depth hD to overturn, given as fraction of crater diameter: $c = 1/2\sqrt{1-h} = 0.41$ (see Figure 1; Costello et al., 2018).

We use the secondary production model published in Costello et al. (2018). Costello et al. (2018) used the results from the (McEwen et al., 2005) study of Mars’ Zunil crater and the work of Shoemaker (1965) to model the production of secondary craters by a primary flux. Following Costello et al. (2018), we assume that every primary impact produces 100,000 secondary impacts: if the impact flux has the shape: ad^b , where d is the impacting fragment diameter and the secondary flux parameter $a_{\text{Secondary}} = a_{\text{Primary}} \times 10^5$. The secondary flux power index is $b_{\text{Secondary}} = -4$ (following Table 4 of McEwen et al., 2005). To produce a secondary CPF we

Table 1

Impactor Size to Crater Size Scaling Parameters From Material Published Online by Holsapple (2003) and From Table 1 in Williams et al. (2014), Which Supersede the Values in Table 1 of Holsapple (1993)

Target material	K_1	K_2	K_d	K_r	μ	Y (dynes cm^{-2})	ρ_i (g cm^{-3})	ρ_t (g cm^{-3})
Regolith	0.132	0.26	1.1	0.6	0.41	1×10^5	1.5	2.7 ^a
Hard ice	0.095	0.351	1.1	0.6	0.55	1.5×10^5	0.93	0.93 ^b

The impactor density for rocky secondaries, following Costello et al. (2018). The impactor density for icy secondaries.

process the flux of secondary fragments through the Holsapple (1993) scaling from impactor size to crater size, assuming that all secondary impactors strike the surface at an average velocity of 0.5 km s^{-1} (Melosh 1985; Vickery, 1986) and the material properties defined in Table 1.

3. Validation: Gardening Regolith on the Moon

3.1. Validation of the Secondary CPF

We test the validity of our assumptions about the scaling from impactor size to crater size, material properties, and the production of secondary crater by calculating gardening due to the crater production observed by the LRO Camera (LROC) over the last decade (Speyerer et al., 2016). The observed CPF by Speyerer et al. (2016) is free from assumptions about material properties, secondary flux, and impact velocity because values for u and v are taken from the size-frequency distribution of observed meter-scale surface albedo anomalies that appeared over the decade LRO has been in orbit. We plot the CPF, equation (5), using shape parameters from the observed distribution of splotches ($u = 1.25 \times 10^{-5}$ and $v = -4.14$ in units of meters and years; these values are reported in the Methods section of (Speyerer et al., 2016) and our parameter-intensive model for the production of secondaries (equation (13)) and note the similarity between these two production functions (Figure 3). Some debate remains about whether albedo anomalous “splotches” observed by LROC are primary or secondary in nature (Speyerer et al., 2016); however, the relatively good fit between our secondary production model and the reported production of splotches suggests that the splotches are indeed secondary.

3.2. Validation of Gardening Model

Our model for the gardening of regolith by primary and secondary craters yields a curve that represents the deepest depth that has been disturbed at least n times with some probability following the cumulative Poisson distribution over a time interval. Canonically, the vertical extent of the percolation of surface-correlated materials has been called the “in situ reworking depth” (see Morris (1978) and this depth defines the lower limit of the “in situ reworking zone” which has an upper limit being the very surface. The number of overturns implied by an in situ reworking depth is a minimum of at least one overturn. More than one overturn can occur in the reworking zone.

We model the in situ reworking depth and zone using our overturn model at high probability. In Figure 4 we compare the model results produced by the updated model presented here, the results of Costello et al. (2018), and the in situ reworking depth observed in Apollo cores (Blanford, 1980; Morris, 1978). To calculate the colored contours we solve equation (9) with values for u and v calculated using equation (13) (which include assumptions about material properties, gravity, velocity, impact angle, and the scaling from impactor size to crater size) for impacts into lunar regolith and the flux of secondary impactors produced by a lunar-scaled Brown et al. (2002) meteorite flux. We assume that the modern flux captured by Brown et al. (2002) has been stable for the last 1 Gyr (e.g., Neukum et al., 2001; Huang et al., 2018). The contours labeled “LROC CPF” are calculated using CPF values for u and v following values reported in Speyerer et al. (2016) for the production of splotches and scaled to transient crater diameter by a factor of 0.84 (Melosh, 1989; Methods section of Speyerer et al., 2016). The gardening from splotches are calculated using only the observed size-distribution of craters and are free from assumptions about material properties or gravity of the target, the velocity, angle of impact or material properties of impactors or pi-crater scaling.

The lunar in situ reworking depth we calculate using our model for secondary production using lunar regolith material properties (Table 1), a modeled secondary impact flux produced by the primary impact flux following Brown et al. (2002), for $n \geq 1$ at 99% probability, is plotted as a red line in Figure 4 and is written explicitly as follows:

$$\Lambda = \begin{cases} 3.94 \times 10^{-5} t^{0.5} & \text{in Strength regime} \\ 7.35 \times 10^{-4} t^{0.35} & \text{in Gravity regime} \end{cases} \quad (14)$$

where t is in units of years and Λ is in units of meters.

The overturn depth function for $n \geq 1$ at 99% probability calculated using the CPF from Speyerer et al. (2016) is written:

$$\Lambda = 3.45 \times 10^{-5} t^{0.47} \quad (15)$$

and is also plotted in Figure 4 as a solid black line. The relatively good fit between these two calculations follows the good fit between the input production functions (Figure 3).

Morris (1978) and Blanford (1980) calculated the depth of the in situ reworking zone by analyzing the depth distribution of surface-correlated space weathering products (I_s/FeO , cosmic ray tracks, and cosmogenic radionuclides; e.g., Fruchter et al., 1976, 1977, 1978) in Apollo drill cores. Upon publication of Morris (1978), no impact gardening model could fit the predicted reworking rate (Arnold, 1975; Gault et al., 1974; see Figure 2 of Morris, 1978) even given low probability, likely because these models did not include gardening due to secondary impacts. The absence of secondary impacts was noted as a likely cause of the misfit by Morris (1978). Morris (1978) somewhat arbitrarily ascribed a 50% probability to his calculations of the in situ reworking depth, reasoning that impact gardening is a stochastic process and noting the absence of further models or observational constraints.

Our model, which includes secondary impacts, and our model of mixing driven by splotches fit using high probability (99% probability of at least 1 overturn, Figure 3). We also see a gradient in the frequency of overturn that fits the variable overturn seen within the in situ reworking zone, with greater frequency at shallower depths. After 500 Myr of gardening, a core that samples the top meter would show an in situ reworking depth of less than a meter, with an in situ reworking zone, where frequent churning has distributed space weathering products into the top 10 cm or so. Most of the Apollo cores have on the order of ten distinct layers—for example, the 236-cm-deep Apollo 15 sample 15001-15006 has 42 distinct textural units (Heiken et al., 1973, 1976), Apollo 12 sample 12025-12028 has 10 (e.g., Fryxell & Heiken, 1974) and concentrations of nano-phase iron, a space weathering product, are typically concentrated in the top 10 cm (Lucey et al., 2006); however, investigations of grain size and sorting within layers and the depth-distribution of space weathering products tell a story of frequent overturns and a complicated history of mixing (e.g., Huang et al., 2017; Lucey et al., 2006; Morris et al., 1979). The fit of our models at high probability and the reasonable gradient in the number of turns we predict compared to the in situ reworking zone analyzed by Morris (1978) and Blanford (1980) support the notion that the work by Morris (1978) may be more representative of global impact gardening than the author gave himself credit. Still, as Morris (1978) stated, a direct and rigorous treatment in which values of reworking depth for various probability levels and number of overturns are determined awaits a much larger database of cores and experiments.

3.3. The Timescale for Validity of the Poisson Model for Secondaries

Awaiting a more complete dataset, our updated model for the depth of impact gardening using the LROC CPF and the model results calculated from the flux of secondary impactors fit both one another and the in situ reworking depths calculated from analysis of Apollo cores by Morris (1978) and Blanford (1980). The fit validates our model for the 1 to 500 Myr timescale over which the Apollo core analysis is representative of the in situ reworking depth.

To calculate the secondary flux we assume that the modern primary impact flux captured by Brown et al. (2002) at the Moon has been stable over the last 1 Gyr (e.g., Neukum et al., 2001; Huang et al., 2018); however, recent work suggests that there may have been an order of magnitude uptick in the flux about 200 Myr ago (Mazrouei et al., 2019). Variations in the impact flux translate directly to variations in the rate of impact gardening. Our model does not currently take in representations of the flux over time that are more sophisticated than a power law; however, given the relatively good fit between the reworking rate over the last 1 Gyr calculated from Apollo cores and our model calculations (Figure 4), the power law appears to be a reasonable approximation.

Primary crater formation is a Poisson process, and generally satisfy the assumptions: (1) craters are uniformly distributed over the surface and through time; and (2) the formation of one crater does not affect the probability of the formation of another. Secondary impacts are not a Poisson process, having a spatial and temporal distribution that is existentially linked to their parent primary impact; however, over long timescales, secondaries become approximately like a Poisson point process. We explore the minimum length of time over which we can comfortably use our model of secondaries as an approximate Poisson process by

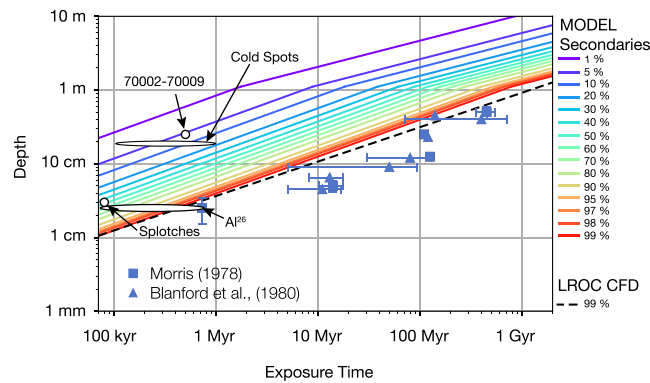


Figure 5. The results of Morris (1978) and Blanford (1980) represent the reworking depth generally; however, the effects of reworking observed in Apollo cores is variable. (i) We capture the stochasticity of gardening by varying the model with probability. At various probabilities, our model is consistent with the reworking demonstrated by the work from Morris (1978) and Blanford (1980); the reported 2 to 3 cm of gardening in 80,000 years from Speyerer et al. (2016) based on observations of the size-frequency of albedo anomalous splotches; the homogenization of o in the top few centimeters of regolith over timescales less than 1 Myr (Fruchter et al., 1976, 1977, 1978); the results of Nishiizumi et al. (2019), who found an event 50 kyr ago overturned about 25 cm of material in Apollo 17 string drill tube 7002-7009; and the fading of thermophysical anomalies dubbed “cold spots” observed in LRO Diviner data that extend to the sensing limit of the diurnal skin depth (20 cm) and are no older than about 1 Myr (Williams, et al., 2018). (ii) The data presented by Morris represents the “in situ reworking depth,” which describes the depth that has seen the surface at least one time over some time interval. Our model results match the Morris (1978) and Blanford (1980) in situ reworking rates, predicting between 1 and 100 overturns have excavated material to the depth and over the timescale.

exploring the timescale over which secondaries begin to behave like a Poisson point process as validated by observations of the effects of gardening in samples and remote sensing observations.

Speyerer et al. (2016) reported a reworking rate of 2 to 3 cm every 80,000 years, which was consistent with the homogeneous distribution of cosmogenic Al^{26} in Apollo cores observed by (Fruchter et al., 1976, 1977, 1978). Our gardening calculations are consistent with this shallow and short-timescale gardening at 50% probability, validating our model for secondary gardening down to the hundreds of thousands of years and centimeter scale. Recent work by Nishiizumi et al. (2019) studying an Apollo 17 drill core 70009-70001 shows an excavation event down to ~ 25 cm occurred about 500 kyr ago. While other cores show that the whole Moon has not been gardened to such depths over hundreds of thousands of years, our model predicts that the Apollo 17 drill core is not wildly anomalous, and suggests that if probability can be linked to spatial coverage, then 5–10% of the lunar surface may have been similarly gardened. The Diviner lunar radiometer experiment on board LRO has also observed ephemeral thermophysical anomalies around young craters that fade over 100 kyr to 1 Myr are at least as thick as the diurnal skin depth: 20 cm (Hayne et al. 2017; Williams et al., 2018). While gardening by secondaries may be only one contributor to the as yet unconstrained mechanisms that destroy cold spots, we see the in situ reworking zone driven by secondaries effecting the total volume of the cold spot at least once at 3% to 20% probability over the timescale of 100 kyr to 1 Myr. We plot our model solved at various probabilities and with these validating observations in Figure 5.

We conclude that secondaries behave like a Poisson point process after about 100 kyr and our model is valid over timescales on and above that order of magnitude. This is not to say that the modeling of secondary impacts as a Poisson point process is without its faults, and we will explore the limitations introduced by this treatment in the discussion section; however, the model fit with observational data suggests that these issues minimally interfere with our predictions at timescales at and above about 100 kyr.

4. Results

4.1. Gardening Ice and Regolith on the Moon and Mercury

With a model validated by the lunar case, we proceed to explore the extent and rate of impact gardening on the Moon and Mercury in both regolith and in ice over timescales between 80,000 and 1 Gyr (Figures 6 and 7). As described in the previous section, we model overturn on the Moon using the primary impactor flux from Brown et al. (2002) scaled to the Moon and the secondary impacts they produce following the method in Costello et al. (2018). We apply this model to Mercury by using the flux of 1 cm to 100 m objects

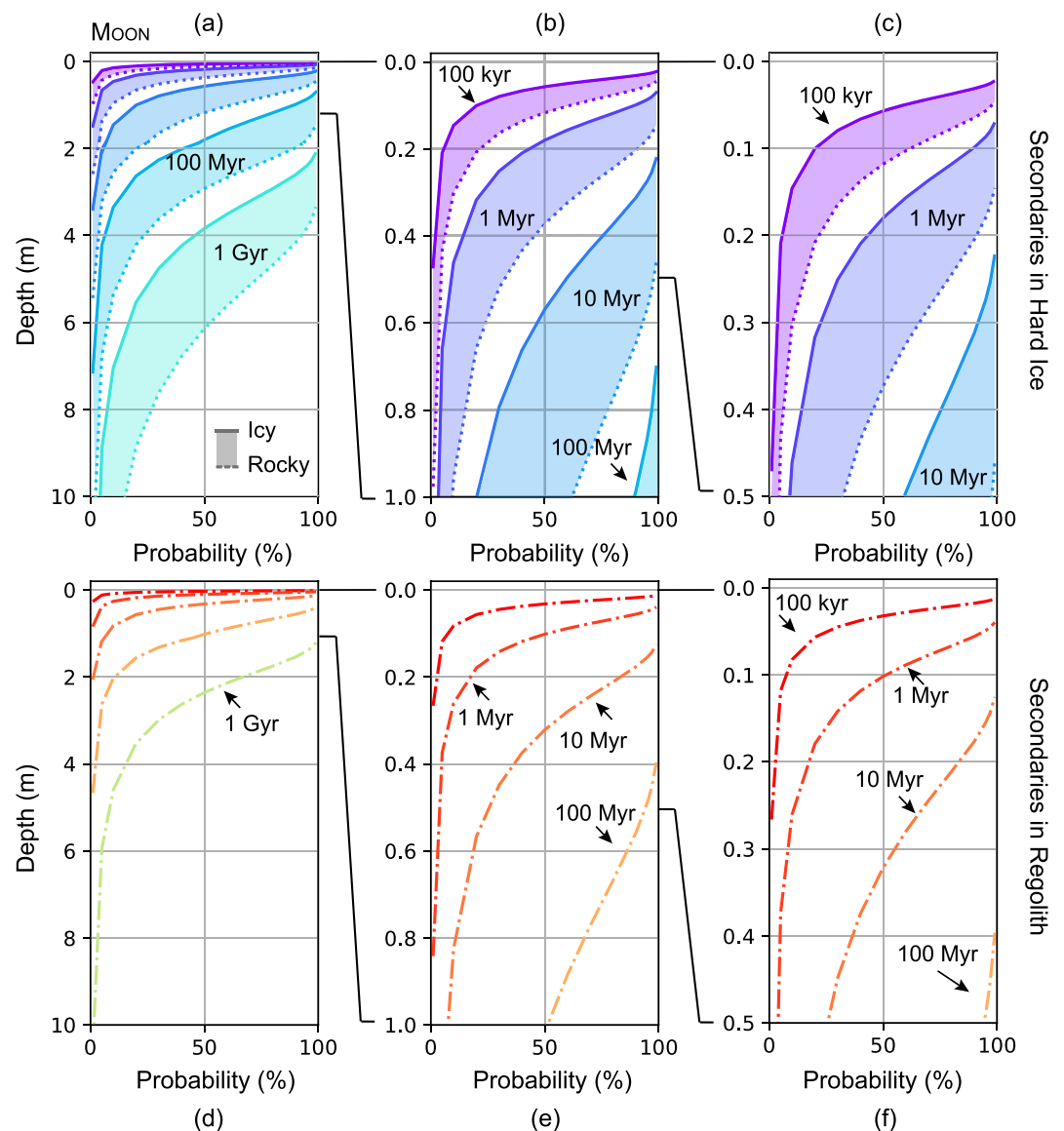


Figure 6. Gardening due to secondary impacts on the Moon in ice and in regolith shown in “cores” that have dimensions of depth and probability. Contours are calculated by solving the cumulative Poisson equation (equation 2) for various probabilities and inputting the appropriate λ into equation (13). We do not include calculations below our reasonable timescale limit of 100 kyr. For our calculation of gardening in an icy target (a, b, and c) we show a region where the true in situ reworking depth likely exists, driven by both icy (solid line) and rocky (dotted line) secondary crater-forming impactors. Similarly, subfigures d, e, and f show gardening depth with varying probability driven by rocky impacts into regolith.

from Marchi et al. (2005). We vary the material property inputs of equations (12) and (13) using values in Table 1 and use the relative gravity of the Moon and Mercury, which control the scaling from impactor size to crater size.

For this study, we make two simplifying assumptions: (1) all craters scale following the Holsapple (1993) scaling laws; and (2) the material being gardened is either pure hard ice or pure regolith. Some workers have shown that transient crater scaling between impactor size and crater size in cold water ice scales like rock in the gravity regime (Chapman & McKinnon, 1986; McKinnon & Parmentier, 1986; Turtle & Pierazzo, 2001). Yet other models and impact experiments suggest that impactor size to crater size scaling may be different in water ice, with differences made more intense as material properties such as porosity evolve with time (Bierhaus & Schenk, 2010; Fendyke et al., 2013; Kurosawa & Takada, 2019; Michikami et al., 2017; Prieur et al., 2017; Yasui et al., 2017). As ice, regolith, and rocks are bombarded, broken, and mixed, the porosity,

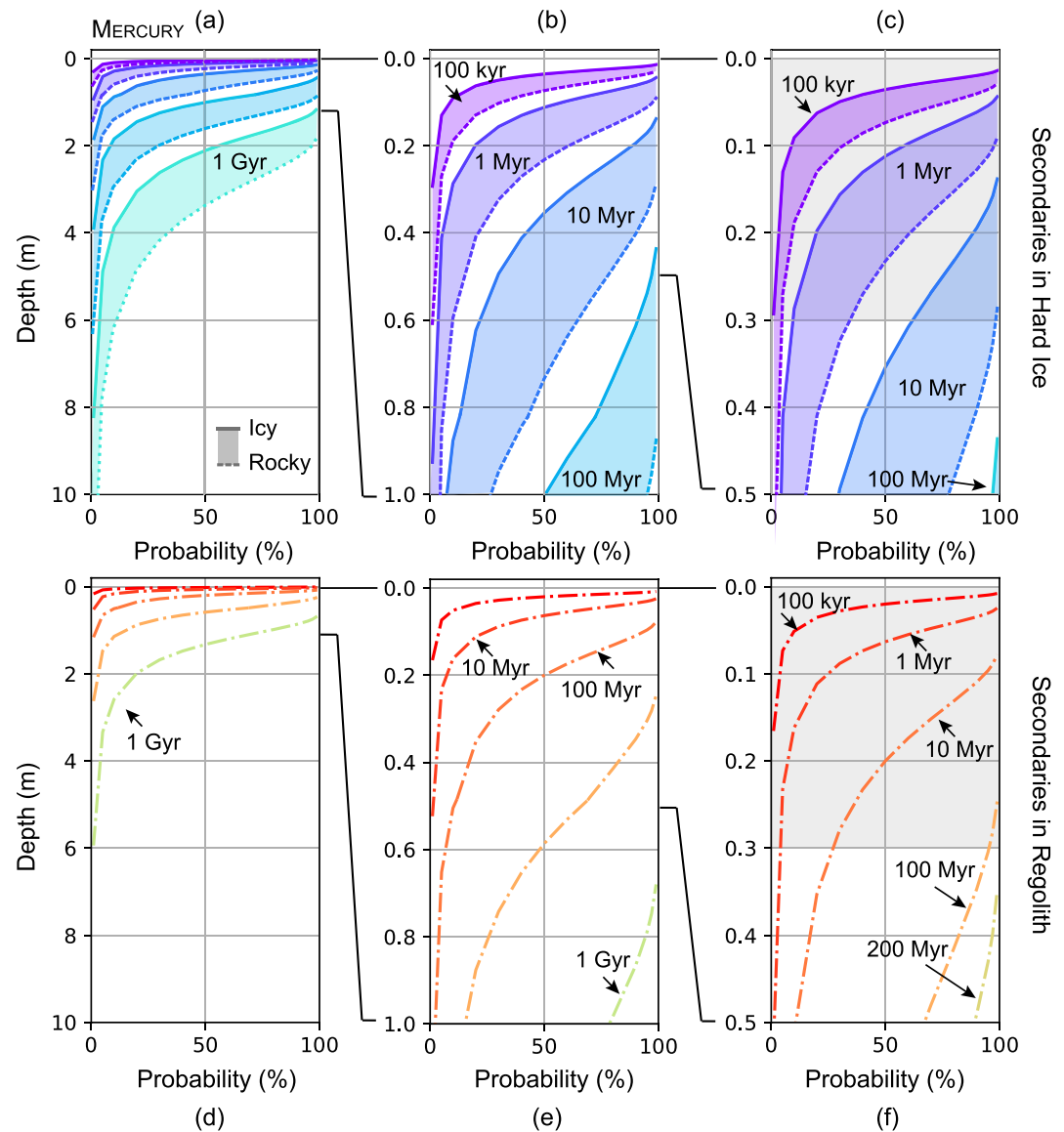


Figure 7. Gardening due to secondary impacts on Mercury in ice and in regolith shown in “cores” that have dimensions of depth and probability. Contours are calculated by solving the cumulative Poisson equation (equation (2)) for various probabilities and inputting the appropriate λ into equation (13). Shaded regions in subfigures (c) and (f) indicate the depth of “microcold traps” and thermal lag deposits, respectively. We do not include calculations below our reasonable timescale limit of 100 kyr. For our calculation of gardening in an icy target (a, b, and c) we show a region where the true in situ reworking depth likely exists, driven by both icy (solid line) and rocky (dotted line) secondary crater-forming impactors. Subfigures d, e, and f show gardening depth driven by rocky impacts into regolith on Mercury.

yield strength, and density of the target evolve with time in poorly constrained ways. We simplify, using the two examples of hard ice and regolith because their material parameters are provided by Holsapple (1993) and are self-consistent with the scaling laws we also take from Holsapple (1993). Including a sophisticated treatment of icy crater scaling and time-dependent surface evolution are beyond the scope of this study.

Overturn functions plotted in Figure 8 are summarized in Table 2 and plotted in Figure 8 for comparison. For overturn in hard ice on both the Moon and Mercury we assume that secondary impactors have the density of ice or rocks (Table 1). Secondaries are more likely to be composed of the same material as the target because of the relatively limited area over which secondaries are strewn, especially at the submeter scales we are modeling, and Mercury’s icy poles are not covered in rocky regolith ejecta; however, the majority of the Moon and Mercury are not icy and it is possible that nonlocal rocky secondaries are making craters in

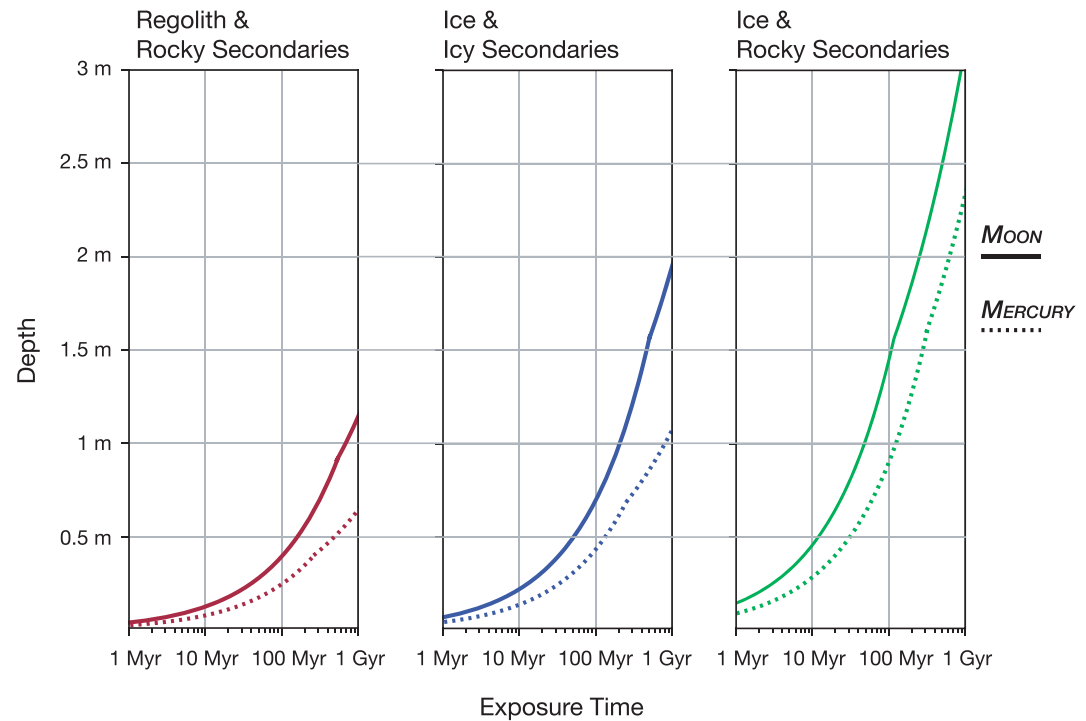


Figure 8. Impact gardening on the Moon and Mercury and regolith and ice due to icy and rocky secondary impactors. Gardening is more efficient on the Moon than Mercury at the depth scale analyzed here (< 10 m), and gardening is more efficient in ice than in regolith on both planetary bodies.

polar ice deposits. The scale of a crater is dependent on the density and yield strength of both the target and impactor. Icy impactors garden less efficiently than rocky impactors due to their lower density and yield strength relative to rocky impactors. By modeling gardening driven by both rock and icy secondaries we present bounds for the upper (all rocky secondaries) and lower (all icy secondaries) limits for gardening at the poles. These limits appear as solid (all icy) and dotted (all rocky) contours bounding a shaded region where the true in situ reworking depth contour, which is likely driven by a mix of rocky and icy secondaries exists in Figures 6 and 7, which illustrate the depth of gardening on the Moon and Mercury respectively. We compare gardening on the Moon and Mercury in Figures 6–8. The figures illustrate two simple and important results: (1) impact gardening at the depth scale modeled here (< 10 meters) is more intense on the Moon than on Mercury by a factor of ~ 2; and (2) on both the Moon and Mercury, hard ice is gardened more efficiently than regolith.

4.2. The Ancient Lunar Flux and Regolith Thickness as a Constraint on Primordial Ice

The Moon may have had extensive Mercury-like ice deposits that have been destroyed or churned into underlying regolith by impact gardening. To explore this hypothesis and the evolution of lunar ice, we investigate

Table 2

Overturn Depths Are Calculated Using Equation (8) for $n \geq 1$ Overturns at 99% Probability and Using the Material Properties Listed in Table 1 and in Hard Ice Given Rocky and Icy Secondary Impactors

	Overturn Depth (Λ)			
	Regolith target		Hard ice target	
	Rocky secondaries		Icy secondaries	Rocky secondaries
Moon (strength regime)	3.94×10^{-5}	$t^{0.5}$	6.97×10^{-5}	1.45×10^{-4}
Moon (gravity regime)	7.35×10^{-4}	$t^{0.32}$	2.44×10^{-3}	3.90×10^{-3}
Mercury (strength regime)	2.45×10^{-5}	$t^{0.5}$	4.33×10^{-5}	8.99×10^{-5}
Mercury (gravity regime)	4.13×10^{-4}	$t^{0.32}$	1.34×10^{-3}	2.92×10^{-3}

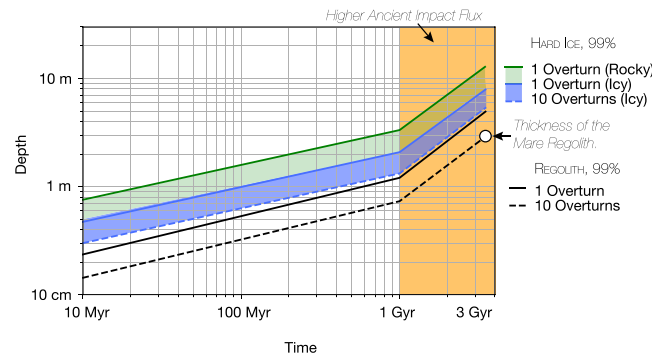


Figure 9. The higher ancient impact flux simulated using the depth of mare regolith. We model impact gardening in regolith and ice for $n \geq 1$ and $n \geq 10$ overturns at 99%. If we assume that between 1 and 10 overturn events in the model transforms mare basalt into regolith, then we can assume that between 1 and 10 overturns have also affected polar ice deposits to a greater depth proportional to the greater efficiency of cratering in ice.

the minimum thickness of lunar ice deposits would have to have been gardened into underlying regolith.

To investigate the effects of gardening on ice deposits that may be older than the Copernican era, we assume that the thickness of mare regolith of known surface age can constrain the unknown thickness of polar ice deposits of the same age. Over the last 3.5 Gyr, impacts have pulverized mare basalts into a regolith layer that is about 3 m thick (Fa & Wieczorek, 2012; Fa et al., 2014, 2015; Bart, 2014; Nakamura et al., 1975). In Figure 9 we extend our model for gardening beyond the Copernican era and explore how thick an ancient pure ice deposit must have been to have been completely penetrated by impacts. We assume that a model for $n \geq 10$ overturns at 99% probability, represents the relatively uniform production of 3 m of mare regolith. We then assume that $n \geq 1$ overturns have also affected polar ice deposits to a greater depth proportional to the greater efficiency of cratering in ice. Under these assumptions, model results indicate that a deposit that is 3.5 Gyr old would have to have initially been 4–15 m thick to be gardened into underlying regolith (Figure 9).

5. Discussion

5.1. The Age of Ice Deposits on Mercury

After 1 Gyr of bombardment, impact gardening is extremely unlikely to have touched the bottom of a 4 to 8 m thick ice deposit on Mercury, let alone deposits greater than 10 m thick (Figure 7a). Our gardening calculations at this millimeter scale do not rule out the possibility that Mercury's extensive ice deposits are older than 1 Gyr.

5.1.1. Shielding by Thermal Lag

Many of Mercury's radar-bright ice deposits are covered by a layer of low-reflectance material that has been interpreted to be the carbonaceous leftovers of ice that has sublimated or “thermal lag” (Crites et al., 2013; Delitsky et al., 2017; Neumann et al., 2013; Paige et al., 2013; Syal et al., 2015). MESSENGER neutron data and thermal models show that these low albedo lag deposits are up to 10–30 cm thick (Lawrence et al., 2013; Paige et al., 2013), and images indicate that the low-reflectance deposits directly overlie ice deposits, terminating sharply at the boundary of radar-bright regions (Chabot et al., 2014).

Impact gardening over the scale of tens of millions of years will only turn up more lag deposit, gardening the first few decimeters of material at Mercury's poles (Figures 6e and 6f). Some impacts will dig deeper; for example, we predict that there is a 50% chance that ice buried under ~ 20 cm of thermal lag will have been excavated once over 10 Myr. Much as Apollo core 7002-7009 showed an anomalously young deeply penetrating impact (Nishiizumi et al., 2019; Figure 5), rare, larger impacts on Mercury may penetrate the lag and exhume small amounts of ice onto the surface, causing observed variations in surface brightness among thermal lag regions (Chabot et al., 2013, 2014; Deutsch et al., 2016). Quantitatively linking the efficiency of lag-penetrating impacts and up-sampling of ice at low model probability and the surface albedo variations awaits a more complete dataset. We can comfortably conclude that shielding by thermal lag further extends the potential lifetime on Mercury's polar ice deposits against gardening. Our model predicts that low-albedo

thermal lag deposits may not only shield the ice deposits they overlie from sublimation (Paige et al., 2013), but also take the brunt of impact gardening.

5.1.2. Age Constraints From Surface Ice

There are locations where temperatures are cold enough that sublimation could not build up a protective blanket of lag and where ice is exposed directly to the surface (Deutsch et al., 2017; Paige et al., 2013). Surface ice is exposed to nonthermal loss processes including sputtering by solar wind plasma, UV, impact vaporization and mechanical gardening that churns protected ice upward to the relatively hostile surface (e.g., Farrell et al., 2019). If exposed ice deposits on Mercury were billions of years old and never developed a shield of thermal lag, they would have succumbed to nonthermal losses. The presence of surface ice implies that the ice deposits on Mercury may indeed be young.

Thermal modeling by Rubanenko et al. (2018) hypothesized the presence of “microcold trap” surface ice deposits existing in submeter regions of permanent shadow that may only be a few decimeters thick. The relative efficiency of gardening in ice makes these small unprotected deposits particularly vulnerable and we predict that if they exist, micro cold trap ice deposits would be thoroughly gardened over 10 Myr timescales (Figure 7c).

5.1.3. Constraints on the Age of Mercury's Ice From Low Albedo Deposits That Are Not Radar-Bright

There also are PSR locations somewhat farther from the poles of Mercury where the surface has low albedo compared to surrounding regolith but is not radar-bright. It is thought that these locations once harbored ice deposits that have since succumbed to thermal sublimation (Paige et al., 2013). If thermal lag at these locations is underlain by regolith, impact gardening will mix them into background regolith over time, much as gardening does to lunar surface features. We assume that the thermal lag deposits are 10–30 cm thick (Lawrence et al., 2013; Paige et al., 2013) and have similar material properties to the surrounding regolith to calculate the depth reached by overturn. In order for us to still be able to observe the low surface albedo anomalies today, they must be too young to have been worked into background regolith by gardening. We predict that it would take less than 200 Myr to mix 30-cm thermal lag underlain by regolith into the background (Figure 7f). Thus, if the albedo-dark deposits are the thermal lag of a sublimated ice deposit, the initial deposition of ice must have occurred no more than 200 Myr ago. The 100 Myr timescale we predict for the gardening of Mercury's lag deposits is three orders of magnitude above the 100 kyr minimum timescale above which our model for secondary impact gardening is valid, so we can be relatively certain of our prediction that Mercury's most recent large scale deposition of ice occurred no more than 200 Myr ago.

Because of its extensive and optically immature rays (Braden & Robinson, 2013; Neish et al., 2013), it has been suggested that Hokusai crater (57.7°N, 16.8°E) formed in the Kuiperian time-stratigraphic system, and has an upper limit age of 100 to 300 Myr (Banks et al., 2017). Our gardening calculations support the narrative of Hokusai as a source for Mercury's most recent large scale ice delivery, by showing that the most recent emplacement must have occurred no more than 200 Myr ago.

5.2. The Sources of Water Delivered to the Moon and Mercury

Surface ice is subject to intense gardening over short timescales (Figures 6c and 7c). The relatively high rate of impact gardening near the surface means that the deposition rate of ice has a major impact on its survival. Ice deposits formed from the steady accumulation of thin layers of water ice from water-bearing meteorites (e.g., Moses et al., 1999) or solar wind implantation (e.g., Crider & Vondrak, 2000) are more vulnerable to the destructive effect of impacts near the surface. Although thin deposits are vulnerable, gardening quickly loses efficiency at depth. A 10 cm thick ice deposit is exponentially more durable against gardening than a 1 cm deposit.

Moses et al. (1999) assumed a dust flux at Mercury of $1 \pm 0.8 \times 10^{10} \text{ g yr}^{-1}$ that contains a water mass fraction of roughly 10%. They assume 63% of the dust flux mass remains on the planet after an impact and 5.15% of the water survives migration to the poles. This produces a cumulative delivery of 0.8 to 20 m of ice to Mercury's poles over 3.5 Gyr with a linear continuous deposition rate of 2.29×10^{-10} to $5.79 \times 10^{-9} \text{ m yr}^{-1}$. Modeling by Ong et al. (2010) shows that about 6.5% of a cometary impact into the Moon is retained, so the lower end of the retention percent used by (Moses et al., 1999) is more likely. Other studies of comet impacts have shown that retention of meteoritic water depends strongly on impact velocity and impact angle—slower and more oblique impacts have less energetic volatile plumes, more of which remain gravitationally bound

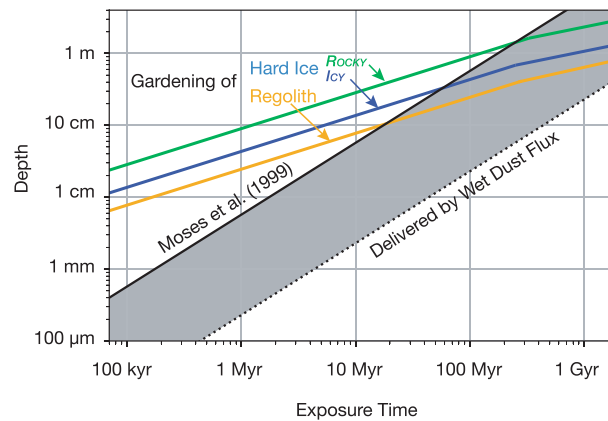


Figure 10. The depth of an ice deposit in the absence of losses or transport after deposition if it were supplied at the rate calculated by Moses et al. (1999) and impact overturn depth contours for impact gardening in regolith and in hard ice due to icy and rocky secondary impactors on Mercury (Table 2). Gardening mixes incrementally built-up deposits formed from continuous sources faster that they are supplied.

(Gisler et al., 2006; Ong et al., 2010; Pierazzo & Melosh, 2000; Prem et al., 2015; Stewart et al., 2011). At Mercury, micrometeorites have a high average impact velocity relative to meteorites larger than ~ 1 g (Cintala, 1992; Marchi et al., 2005), and their vapor plumes are less likely to be low energy enough for water to remain gravitationally bound. Considering these factors, we should think of the Moses et al. (1999) supply as a generous estimate.

We compute the depth that an ice deposit would be in the absence of any losses if it were supplied by meteorites at the generous rate calculated by Moses et al. (1999) and compare it to the overturn depth we calculate, plotting them together in Figure 10. Let us imagine ~ 4 mm of ice accumulates on a patch of ground in a PSR over about 1 Myr. Our model suggests that that patch of ground is gardened to at least 2 cm depth over the same time interval, overturning an order of magnitude more material than the continuous source was able to accumulate. Smaller time steps and thinner deposits are even more vulnerable to the power law efficiency of gardening. The incremental layers built up over time by continuous sources are mixed with underlying regolith faster than they can accumulate, thwarting the growth of a pure ice deposit like those seen at Mercury's poles (e.g., Butler et al., 1993). We conclude from this exercise that pure, many meters-thick ice deposits on Mercury could not have been built over billions of years from continuous sources because impact gardening mixes incrementally built up ice layers with underlying regolith faster than continuous sources can supply them. In contrast, we can not similarly rule out the possibility that lunar ice, which appears to be well mixed with regolith (e.g., Colaprete et al., 2010), may be continuously supplied.

In the previous section we concluded that the presence of albedo-dark lag underlain by regolith implies near-surface ice on Mercury has a maximum age of about 200 Myr. Over 200 Myr, even the ungardened and generous estimate of the amount of water supplied to the poles by wet meteorites (Moses et al., 1999) provides only enough water for a deposit that is a few millimeters thick (Figure 7). If Mercury's pure ice deposits are indeed less than 200 Myr old, even in the absence of gardening, the continuous supply calculated by (Moses et al., 1999) could not have made them. The relatively young predicted age of Mercury's most recent ice delivery and the durability of thick deposits in comparison to intensely gardened thin deposits indicate that the sources of ice at the poles of Mercury were voluminous and suddenly delivered, such as a single or a series of large comet impacts. We do not rule out the possibility that Mercury's polar deposits were formed from multiple exogenous and endogenous sources, so long as those sources were relatively sudden and voluminous; for example, an ancient volcanic outgassing (e.g., Butler et al., 1993, 1997) was supplemented by large cometary depositions (e.g., Ernst et al., 2018) with invisible layering of thermal lag at thicknesses below the resolution of radar remote sensing.

While we do not have similar age constraints on lunar ice deposits, the relative durability of thick deposits against gardening supports the theory of a voluminous and sudden source for lunar ice as well. Farrell et al. (2019) concluded that ice on the surface of the Moon may only be stable for < 2 kyr, suggesting an extremely turbulent near surface environment and spelling doom for thin layers of continuously delivered ice. If the

Moon does indeed have pure ice deposits that are buried (e.g., Rubanenko et al., 2019), such deposits would have had to have grown and survived gardening at the surface for some time before their burial, and, like Mercury's deposits, could not have been continuously supplied. Thus, we conclude that a sudden and voluminous source of lunar polar water delivery, such as a volcanic outgassing (e.g., Needham & Kring, 2017), is more likely than continuous supply.

5.3. Ice on the Moon

Gardening is more efficient on the Moon than on Mercury (Figure 8) due to the higher flux of 1 cm to 100 m primary impactors at the Moon (Marchi et al., 2005); however, despite the greater efficiency, gardening would never have penetrated the entirety of a Mercury-like deposit on the Moon if that deposit was < 1 Gyr old. Even a 5 m thick deposit that was emplaced 1 Gyr ago would not have been gardened in its entirety and should still appear radar-bright. If the Moon ever had Mercury-like deposits they must have been ancient (e.g., Deutsch et al., 2019; Needham & Kring, 2017), and therefore subject to the orders of magnitude higher impact environment before the Copernican era or buried.

5.3.1. The Fate of Primordial Surface Ice

We explored the idea of thick primordial deposits in section 4.2, and were able to present a rough estimate of the minimum thickness a surface deposit must have been to have been gardened to its interface with the regolith: 4–15 m. The results suggest that the Moon may well have had ancient Mercury-like deposits that were initially thicker than 10 m which have since succumbed to gardening, which are now so thoroughly mixed with regolith that they are invisible to radar (e.g., Butler et al., 1993; Colaprete et al., 2010).

Our results come from assumptions about the relationship between regolith growth and gardening, but that relationship is itself a subject of ongoing investigation. Hirabayashi et al. (2018) modeled the growth of regolith from high energy primary impacts, not the secondary impacts that we model here, and had model results in good agreement with the regolith depths sensed by Apollo 15 seismic experiments (Nakamura et al., 1975). It is thought that regolith production is driven by high energy impacts (e.g., Hirabayashi et al., 2018; Oberbeck et al., 1973; Quaide & Oberbeck, 1975), by micrometeorite abrasion (e.g., Hörz et al., 1974), and/or thermal fatigue (e.g., Delbo et al., 2014; Molaro & Byrne, 2012; Molaro et al., 2015, 2017) to varying and yet unknown degrees, while gardening is driven mostly by frequent low energy secondary impacts. If the secondary impacts that we model do not possess enough energy to produce 3 m of mare regolith, then the impact flux must have been more than an order of magnitude more intense than that modeled here, ancient ice deposits would have had to be much thicker, and thicker deposits mean a greater mass is demanded from any delivery mechanism. A better understanding of the relationship between regolith production and mechanical churning would improve our ability to derive the initial thickness of ice deposits from the depth of similar-aged regolith and interpret model results.

Our results suggest that the top meter or so of Mercury is less reworked than the top meter of the Moon. The relatively slower processing of the top few meters of Mercury's surface is consistent with observations that ice deposits on Mercury have a sharp boundary with their surroundings (e.g., Chabot et al., 2014); however, studies suggest that Mercury has thicker regolith than the Moon (Kreslavsky & Head, 2015) and that craters degrade faster on Mercury than on the Moon (Fassett et al., 2017). Again, we run into the uncertain relationship between impact gardening and regolith formation. We look forward to seeing what the Bepi-Colombo mission to Mercury reveals about the small impactor flux at Mercury and the results of continuing studies of the relationship between impacts, regolith growth, and crater degradation. For now, we proceed under the assumption that the Marchi et al. (2005) flux of 1 cm to 100 m objects is correct and is indeed driving the relatively slow gardening of Mercury's top meter.

5.3.2. The Depth to Buried Ice

If instead of extensive Mercury-like surface deposits, ancient lunar ice was buried under meters of regolith (e.g., Rubanenko et al., 2019), and if cohesive ice deposits exist at depths between 1 and 10 m, the surface ice we observe may be the result of secondary impact gardening up-sampling that ice during the Copernican era. Our gardening calculations at high probability give a lower limit on the depth of up-sampled ice. Any shallower than our calculations, and buried ice would have been gardened in the in situ reworking zone. We predict that gardening could efficiently up-sample ice when it is touched by the in situ reworking depth; thus, ice may be buried between 1 cm and 3 m deep (from interpretation of Figures 4 and 6). Such shallow deposits should be visible to radar; however, the radar remains dark.

The observed surface ice may be the result of rare, relatively large impacts which penetrate a deep regolith layer. We can investigate this possibility by exploring the depth to ice using lower probability in the model. We performed a similar exercise using lower probability to explore the mixing history of Apollo core 70002-70009 Nishiizumi et al. (2019) and the fading of cold spots Williams et al. (2018) in section 3.1. If we accept that gardening at 10% probability accounts for the observed surface ice, buried ice may be between 10 cm and approaching 10 m deep (Figures 5 and 6). How so much regolith was deposited over the purported buried ice deposits while similarly-aged pyroclastic deposits such as those at Aristarchus remain spectrally distinct at the surface (e.g., Lucey et al., 1986) remains an open question.

While Figures 6 and 7 and the gradient of probability that they illustrate could be interpreted to be representative of the depth to ice on the Moon and Mercury, we caution the reader that interpretation of model results at low probability introduces both known and unknown unknowns. While the vertical and temporal gardening that our model predicts is in comfortable agreement with several validating observations of the vertical and temporal extent of gardening on the Moon, interpretation from spatial dimensions introduces uncertainty. If we wish to rigorously investigate the observed spatial distribution of surface ice and link it to probability of overturn, we would need to qualify our model with more observational data to illustrate the validity or invalidity of its results for similar applications. We do not know what areal fraction of the lunar surface has a mixing history similar to the Apollo core 70002-70009, or what physical processes fade cold spots, let alone that gardening 10%, 50% or 100% of a cold spot volume fades it and therefore cannot use these as rigorously validating or invalidating cases for the spatial distribution implied by lower percent probability in the model.

One known unknown that we are particularly cautious of is the implications of our model dimensions. Between equations (1) and (3) of this work, we reduce the dimensionality of our marked homogeneous point process intensity function from four (two spatial dimensions, time, and one mark) down to two (time and depth/mark) using the geometry of the problem (Figure 2) and the assumption that the distribution of points and marks are independent. Reducing the dimensionality of a model in this way may make the model blind to pertinent physical phenomena. For example, (Minton et al., 2019) presented both an analytic and a numerical approach to modeling surface degradation by crater equilibrium. Their analytic model had only one dimension: mark. When comparing their analytic results and numerical results, they found the analytic model could not have predicted the significant effects of spatial parameters such as crater ray width, which were not reduced and apparent in their computationally expensive numeric model. Similarly, we should approach the computationally efficient yet dimensionally reduced models presented in this work and by Costello et al. (2018) and Gault et al. (1974) with caution when trying to understand the influence and implications of spatial phenomena beyond the vertical dimension, such as the patchy surface distribution of water, pending further qualification from observations, cores, and experiments that investigate the physical and spatial effects of frequent small scale impacts.

We encounter another issue with our analytic model for secondary cratering when we consider the dynamism of ice on the uppermost lunar surface. Farrell et al. (2019) performed calculations that suggest that what little surface ice exists on the Moon remains on the surface for < 2 kyr, and that the surface environment may be extremely dynamic. Impact gardening by secondaries must play some role in the dynamism; however, the 1 kyr timescale is well below our reasonable limit for treating secondaries as a Poisson process, and, in its present form, our model can contribute little of value to understanding the evolution of these most ephemeral deposits.

In the future it will be valuable to develop the models used in this work further. By updating the model we may be able to avoid reducing dimensions and constrain the shallowest and most ephemeral impact gardening. An improved model for secondary crater production that can accommodate differences in the production of secondaries driven by the material properties of the body (e.g., ice vs. silicate worlds), gravity, and velocity of impacts may also significantly improve these results, especially as we explore further beyond the Moon (e.g., Bierhaus et al., 2018).

6. Conclusions

The updated model fit well with the extent of impact gardening in Apollo cores (Blanford, 1980; Morris, 1978), and calculated from the size frequency distribution of albedo-anomalous splotches in LROC temporal pairs (Speyerer et al., 2016). The fit between our secondary crater production model and the production of

albedo anomalies observed in LROC temporal pairs from (Speyerer et al., 2016), or splotches, implied that the splotches are indeed secondary cratering phenomena. We validated the impact gardening model for the Moon in regolith for timescales between 100 kyr and 500 Myr.

With a validated model in hand, we modeled the gardening of hard ice and regolith on the Moon. Ancient polar ice would have been subject to a similar impact flux as mare basalt, and because mare basalts were pulverized into ~ 3 m of regolith, ice at the poles must have been gardened to a similar or greater depth based on the relative efficiency of cratering in ice compared to rock and regolith. We tracked the relatively higher efficiency of gardening in ice and conclude that if ice was emplaced in lunar polar PSRs 3.5 Gyr ago, the deposits may have been 4–15 m thick.

Unlike the Moon, Mercury's present ice is abundant. While our model can not rule out an ancient origin for Mercury's deep deposits directly from gardening because of their extensive depth and shielding by thermal lag, the presence of surface ice suggests a recent delivery. We can further constrain the age of Mercury's most recent large-scale delivery of ice by modeling the gardening of lower latitude albedo-dark features that have been interpreted to be the remains of ice deposits that have sublimated. Because we still observe these albedo-dark features, they must not yet have been gardened into background regolith and we predict that the ice that preceded them must have been emplaced no more the 200 Myr ago. This timescale is consistent with the Hokusai impactor being the most recent large-scale delivery of water (Ernst et al., 2018).

Moses et al. (1999) calculated a generous estimate for the amount of water delivered to Mercury's poles by continuous supply. Even this generous estimate of the continuous delivery of water from micrometeorites only emplaces several millimeters of ice over 200 Myr. Ice deposits from continuous supply take time to grow—and during that time they are subject to intense small-scale impact gardening. It is unlikely that significant ice deposits on either the Moon or Mercury are the result of a continuous supply of water. Prompt and voluminous sources such as cometary impact are exponentially more durable against gardening. The ice observed on the Moon and Mercury is therefore more likely to have had a prompt and voluminous source or sources (e.g., large cometary impacts, such as the Hokusai impact on Mercury less than 200 Myr ago Ernst et al., 2018), or voluminous ancient volcanic outgassing (e.g., Kerber et al., 2009; Needham & Kring, 2017) to withstand intense small-scale gardening.

We conclude that the difference between the water distribution at the poles of the Moon and Mercury is driven by luck and gardening. Mercury was struck in the last 200 Myr by a rare and large water-bearing object that deposited a significant amount of water. Mercury may already have had extensive ice deposits built up from other cometary impacts and/or a primordial outgassing that had not been significantly gardened due to the relatively lower impact flux of 1 cm to 100 m objects (Marchi et al., 2005). Over the last billion years, Mercury's ice deposits have only needed to contend with a modern flux that is gentle relative to both the ancient and modern lunar flux, and are widely shielded from gardening and surface loss processes by decimeter-scale thermal lag deposits. Although the gardening rate is higher on the Moon, if a Mercury-like mass of water had been placed on Moon during the Copernican era, its remains should still be radar-bright today. Instead, we observe a comparatively dry Moon. In the future, the differences between the poles of the Moon and Mercury will likely become even more pronounced, as gardening continues to contribute to the depletion of what ice remains on the Moon and only scratches the surface of Mercury's extensive deposits.

Acknowledgments

Work described in this paper was sponsored in part by the National Aeronautics and Space Administrations Lunar Reconnaissance Orbiter project under a contract to the University of California at Los Angeles (David A. Paige, Principal Investigator) and by support from a Bullard Fellowship Award through the University of Hawaii. M. H. acknowledges support from Auburn University's Intramural Grant Program. We give special thanks to David Minton (Purdue University) and Ya-Huei Huang (Massachusetts Institute of Technology), whose expert advice on modeling cratering processes greatly improved this work. All of the data produced and plotted in this work can be reproduced using the equations and parameters provided.

References

- Arnold, J. R. (1975). Monte Carlo simulation of turnover processes in the lunar regolith. In *Lunar and Planetary Science Conference Proceedings* (Vol. 6, pp. 2375–2395).
- Banks, M. E., Xiao, Z., Braden, S. E., Barlow, N. G., Chapman, C. R., Fassett, C. I., & Marchi, S. S. (2017). Revised constraints on absolute age limits for Mercury's Kuiperian and Mansurian stratigraphic systems. *Journal of Geophysical Research: Planets*, 122, 1020. <https://doi.org/10.1002/2016JE005254>
- Bart, G. D. (2014). The quantitative relationship between small impact crater morphology and regolith depth. *Icarus*, 235, 130–135.
- Bierhaus, E. B., Chapman, C. R., & Merline, W. J. (2005). Secondary craters on Europa and implications for cratered surfaces. *Nature*, 437(7062), 1125–1127.
- Bierhaus, E. B., McEwen, A. S., Robbins, S. J., Singer, K. N., Dones, L., Kirchoff, M. R., & Williams, J. P. (2018). Secondary craters and ejecta across the solar system: Populations and effects on impact-crater-based chronologies. *Meteoritics & Planetary Science*, 53(4), 638–671.
- Bierhaus, E. B., & Schenk, P. M. (2010). Constraints on Europa's surface properties from primary and secondary crater morphology. *Journal of Geophysical Research*, 115, E12004. <https://doi.org/10.1029/2009JE003451>
- Blanford, G. E. (1980). Cosmic ray production curves below reworking zones. In *Lunar and Planetary Science Conference Proceedings* (Vol. 11, pp. 1357–1368). New York: Pergamon Press.

- Boynton, W. V., Droege, G. F., Mitrofanov, I. G., McClanahan, T. P., Sanin, A. B., Litvak, M. L., & Harshman, K. (2012). High spatial resolution studies of epithermal neutron emission from the lunar poles: Constraints on hydrogen mobility. *Journal of Geophysical Research*, *117*, 1991–2012. <https://doi.org/10.1029/2011JE003979>
- Braden, S. E., & Robinson, M. S. (2013). Relative rates of optical maturation of regolith on Mercury and the Moon. *Journal of Geophysical Research: Planets*, *118*, 1903–1914. <https://doi.org/10.1002/jgre.20143>
- Brown, P., Spalding, R. E., ReVelle, D. O., Tagliaferri, E., & Worden, S. P. (2002). The flux of small near-Earth objects colliding with the Earth. *Nature*, *420*(6913), 294.
- Butler, B. J. (1997). The migration of volatiles on the surfaces of Mercury and the Moon. *Journal of Geophysical Research*, *102*(E8), 19,283–19,291.
- Butler, B. J., Muhleman, D. O., & Slade, M. A. (1993). Mercury: Full-disk radar images and the detection and stability of ice at the north pole. *Journal of Geophysical Research*, *98*, 15,003–15,023.
- Campbell, D. B., Campbell, B. A., Carter, L. M., Margot, J.-L., & Stacy, N. J. S. (2006). No evidence for thick deposits of ice at the lunar south pole. *Nature*, *443*(7), 835–837. <https://doi.org/10.1038/nature05167>
- Chabot, N. L., Ernst, C. M., Denevi, B. W., Nair, H., Deutsch, A. N., Blewett, D. T., & Harmon, J. K. (2014). Images of surface volatiles in Mercury's polar craters acquired by the MESSENGER spacecraft. *Geology*, *42*(12), 1051–1054.
- Chabot, N. L., Ernst, C. M., Harmon, J. K., Murchie, S. L., Solomon, S. C., Blewett, D. T., & Denevi, B. W. (2013). Craters hosting radar-bright deposits in Mercury's north polar region: Areas of persistent shadow determined from MESSENGER images. *Journal of Geophysical Research: Planets*, *118*, 26–36. <https://doi.org/10.1029/2012JE004172>
- Chapman, C. R., & McKinnon, W. B. (1986). Cratering of planetary satellites, In *IAU Colloq. 77: Some background about satellites* (pp. 492–580).
- Cintala, M. J. (1992). Impact-induced thermal effects in the lunar and Mercurian regoliths. *Journal of Geophysical Research*, *97*(E1), 947–973.
- Colaprete, A., Schultz, P., Heldmann, J., Wooden, D., Shirley, M., Ennico, K., & Goldstein, D. (2010). Detection of water in the LCROSS ejecta plume. *Science*, *330*(6003), 463–468.
- Costello, E. S., Ghent, R. R., & Lucey, P. G. (2018). The mixing of lunar regolith: Vital updates to a canonical model. *Icarus*, *314*, 327–344.
- Crater Analysis Techniques Working Group (1979). Standard techniques for presentation and analysis of crater size-frequency data. *Icarus*, *37*(2), 467–474.
- Crider, D. H., & Vondrak, R. R. (2000). The solar wind as a possible source of lunar polar hydrogen deposits. *Journal of Geophysical Research*, *105*(E11), 26,773–26,782.
- Crider, D. H., & Vondrak, R. R. (2002). Hydrogen migration to the lunar poles by solar wind bombardment of the Moon. *Advances in Space Research*, *30*(8), 1869–1874.
- Crites, S. T., Lucey, P. G., & Lawrence, D. J. (2013). Proton flux and radiation dose from galactic cosmic rays in the lunar regolith and implications for organic synthesis at the poles of the Moon and Mercury. *Icarus*, *226*(2), 1192–1200.
- Delbo, M., Libourel, G., Wilkerson, J., Murdoch, N., Michel, P., Ramesh, K. T., & Marchi, S. (2014). Thermal fatigue as the origin of regolith on small asteroids. *Nature*, *508*(7495), 233.
- Delitsky, M. L., Paige, D. A., Siegler, M. A., Harju, E. R., Schriver, D., Johnson, R. E., & et al. (2017). Ices on Mercury: Chemistry of volatiles in permanently cold areas of Mercury's north polar region. *Icarus*, *281*, 19–31.
- Deutsch, A. N., Chabot, N. L., Mazarico, E., Ernst, C. M., Head, J. W., Neumann, G. A., & Solomon, S. C. (2016). Comparison of areas in shadow from imaging and altimetry in the north polar region of Mercury and implications for polar ice deposits. *Icarus*, *280*, 158–171.
- Deutsch, A. N., Head, J. W., Chabot, N. L., & Neumann, G. A. (2018). Constraining the thickness of polar ice deposits on Mercury using the Mercury Laser Altimeter and small craters in permanently shadowed regions. *Icarus*, *305*, 139–148.
- Deutsch, A. N., Head, J. W. III, & Neumann, G. (2019). Analyzing the ages of south polar craters on the Moon: Implications for the sources and evolution of surface water ice. *Icarus*, *336*, 113455.
- Deutsch, A. N., Neumann, G. A., & Head, J. W. (2017). New evidence for surface water ice in small scale cold traps and in three large craters at the north polar region of Mercury from the Mercury Laser Altimeter. *Geophysical Research Letters*, *44*, 9233–9241. <https://doi.org/10.1002/2017gl074723>
- Eke, V. R., Lawrence, D. J., & Teodoro, L. F. (2017). How thick are Mercury's polar water ice deposits? *Icarus*, *284*, 407–415.
- Ernst, C. M., Chabot, N. L., & Barnouin, O. S. (2018). Examining the potential contribution of the Hokusai impact to water ice on Mercury. *Journal of Geophysical Research: Planets*, *123*, 2628–2646. <https://doi.org/10.1029/2018JE005552>
- Fa, W., & Cai, Y. (2013). Circular polarization ratio characteristics of impact craters from Mini-RF observations and implications for ice detection at the polar regions of the Moon. *Journal of Geophysical Research: Planets*, *118*, 1582–1608. <https://doi.org/10.1002/jgre.20110>
- Fa, W., Liu, T., Zhu, M. H., & Haruyama, J. (2014). Regolith thickness over Sinus Iridum: Results from morphology and size-frequency distribution of small impact craters. *Journal of Geophysical Research: Planets*, *119*, 1914–1935. <https://doi.org/10.1002/2013JE004604>
- Fa, W., & Wiczeorek, M. A. (2012). Regolith thickness over the lunar nearside: Results from Earth-based 70-cm Arecibo radar observations. *Icarus*, *218*(2), 771–787.
- Fa, W., Zhu, M. H., Liu, T., & Plescia, J. B. (2015). Regolith stratigraphy at the Chang'E-3 landing site as seen by lunar penetrating radar. *Geophysical Research Letters*, *42*, 10,179–10,187. <https://doi.org/10.1002/2015GL066537>
- Farrell, W. M., Hurley, D. M., Poston, M. J., Hayne, P. O., Szalay, J. R., & McLain, J. L. (2019). The young age of the LAMP-observed frost in lunar polar cold traps. *Geophysical Research Letters*, *46*, 8680–8688. <https://doi.org/10.1029/2019GL083158>
- Fassett, C. I., Crowley, M. C., Leight, C., Dyar, M. D., Minton, D. A., Hirabayashi, M., & Watters, W. A. (2017). Evidence for rapid topographic evolution and crater degradation on Mercury from simple crater morphology. *Geophysical Research Letters*, *44*, 5326–5335. <https://doi.org/10.1002/2017GL073769>
- Feldman, W. C., Lawrence, D. J., Elphic, R. C., Barraclough, B. L., Maurice, S., Genetay, I., & Binder, A. B. (2000). Polar hydrogen deposits on the Moon. *Journal of Geophysical Research*, *105*(E2), 4175–4195.
- Fendyke, S., Price, M. C., & Burchell, M. J. (2013). Hydrocode modelling of hypervelocity impacts on ice. *Advances in Space Research*, *52*(4), 705–714.
- Fisher, E. A., Lucey, P. G., Lemelin, M., Greenhagen, B. T., Siegler, M. A., Mazarico, E., & Paige, D. A. (2017). Evidence for surface water ice in the lunar polar regions using reflectance measurements from the Lunar Orbiter Laser Altimeter and temperature measurements from the Diviner Lunar Radiometer Experiment. *Icarus*, *292*, 74–85.
- Fruchter, J., Rancitelli, L., Evans, J., & Perkins, R. (1978). Lunar Surface processes and cosmic ray histories over the past several million years. *Proceedings of the Conference on Lunar and Planetary Science*, *9*, 2019–2032.
- Fruchter, J., Rancitelli, L., Laul, J., & Perkins, R. (1977). Lunar regolith dynamics based on analysis of the cosmogenic radionuclides na-22, al-26, and mn-53. *Proceedings of the Conference on Lunar and Planetary Science*, *8*, 3595–3605.

- Fruchter, J., Rancitelli, L., & Perkins, R. (1976). Recent and long-term mixing of the lunar regolith based on Na-22 and Al-26 measurements in Apollo 15, 16, and 17 deep drill stems and drive tubes. *Proceedings of the Conference on Lunar and Planetary Science*, 7, 27–39.
- Fryxell, R., & Heiken, G. (1974). Preservation of lunar core samples: Preparation and interpretation of three-dimensional stratigraphic sections. In *Proc. Lunar Sci. Conf. 5th*, pp. 935–966.
- Gault, D. E. (1970). Saturation and equilibrium conditions for impact cratering on the lunar surface: Criteria and implications. *Radio Science*, 5(2), 273–291.
- Gault, D. E., Hörz, F., Brownlee, D. E., & Hartung, J. B. (1974). Mixing of the lunar regolith. In *Lunar and Planetary Science Conference Proceedings* (Vol. 5, pp. 2365–2386).
- Gisler, G. R., Weaver, R. P., & Gittings, M. L. (2006). Energy partitions in three-dimensional simulations of the Chicxulub meteor impact. *37th Annual Lunar and Planetary Science Conference* (Vol. 37).
- Harcke, L. J. (2005). *Radar imaging of solar system ices (UMI-31-71807)*. Stanford, CA: Stanford University.
- Harmon, J. K., & Slade, M. A. (1992). Radar mapping of Mercury: Full-disk images and polar anomalies. *Science*, 258(5082), 640–643.
- Harmon, J. K., Slade, M. A., Velez, R. A., Crespo, A., Dryer, M. J., & Johnson, J. M. (1994). Radar mapping of Mercury's polar anomalies. *Nature*, 369(6477), 213.
- Hayne, P. O., Bandfield, J. L., Siegler, M. A., Vasavada, A. R., Ghent, R. R., Williams, J. P., et al. (2017). Global regolith thermophysical properties of the Moon from the Diviner Lunar Radiometer Experiment. *Journal of Geophysical Research: Planets*, 122(12), 2371–2400.
- Hayne, P. O., Hendrix, A., Sefton-Nash, E., Siegler, M. A., Lucey, P. G., Retherford, K. D., & Paige, D. A. (2015). Evidence for exposed water ice in the Moon's south polar regions from Lunar Reconnaissance Orbiter ultraviolet albedo and temperature measurements. *Icarus*, 255, 58–69.
- Heiken, G. H., McKay, D. S., & Fruland, R. M. (1973). Apollo 16 soils: Grain size analysis and petrography. *Proceedings of the Lunar Science Conference*, 4, 251–265.
- Heiken, G. H., Morris, R. V., McKay, D. S., & Fruland, R. M. (1976). Petrographic and ferromagnetic resonance studies of the Apollo 15 deep drill core. *Proceedings of the Lunar Science Conference*, 7, 93–111.
- Hirabayashi, M., Howl, B. A., Fassett, C. I., Soderblom, J. M., Minton, D. A., & Melosh, H. J. (2018). The role of breccia lenses in regolith generation from the formation of small, simple craters: Application to the Apollo 15 landing site. *Journal of Geophysical Research: Planets*, 123, 527–543. <https://doi.org/10.1002/2017JE005377>
- Holsapple, K. A. (1993). The scaling of impact processes in planetary sciences. *Annual review of earth and planetary sciences*, 21(1), 333–373.
- Holsapple, K. A. (2003). *Theory and equations for craters from impacts and explosions*. St. Louis, MO: Washington University.
- Hörz, F., Schneider, E., & Hill, R. E. (1974). Micrometeoroid abrasion of lunar rocks—A Monte Carlo simulation. *Lunar and Planetary Science Conference Proceedings* (Vol. 5, pp. 2397–2412).
- Huang, Y. H., Minton, D. A., Hirabayashi, M., Elliott, J. R., Richardson, J. E., Fassett, C. I., & Zellner, N. E. (2017). Heterogeneous impact transport on the Moon. *Journal of Geophysical Research: Planets*, 122, 1158–1180. <https://doi.org/10.1002/2016JE005160>
- Huang, Y. H., Minton, D. A., Zellner, N. E., Hirabayashi, M., Richardson, J. E., & Fassett, C. I. (2018). No change in the recent lunar impact flux required based on modeling of impact glass spherule age distributions. *Geophysical Research Letters*, 45, 6805–6813. <https://doi.org/10.1029/2018GL077254>
- Hurley, D. M., & Benna, M. (2018). Simulations of lunar exospheric water events from meteoroid impacts. *Planetary and Space Science*, 162, 148–156.
- Ivanov, B. A., Neukum, G., Bottke, W. F., & Hartmann, W. K. (2002). The comparison of size-frequency distributions of impact craters and asteroids and the planetary cratering rate. *Asteroids III*, 1, 89–101.
- Ivanov, B. A., Neukum, G., & Wagner, R. (2001). Size-frequency distributions of planetary impact craters and asteroids. In *Collisional processes in the solar system* (pp. 1–34). Dordrecht: Springer.
- Kerber, L., Head, J. W., Solomon, S. C., Murchie, S. L., Blewett, D. T., & Wilson, L. (2009). Explosive volcanic eruptions on Mercury: Eruption conditions, magma volatile content, and implications for interior volatile abundances. *Earth and Planetary Science Letters*, 285(3), 263–271.
- Kreslavsky, M. A., & Head, J. W. (2015). A thicker regolith on Mercury. In *Lunar and Planetary Science Conference*, 46, 1246.
- Kurosawa, K., & Takada, S. (2019). Impact cratering mechanics: A forward approach to predicting ejecta velocity distribution and transient crater radii. *Icarus*, 317, 135–147.
- Lawrence, D. J., Feldman, W. C., Goldsten, J. O., Maurice, S., Peplowski, P. N., Anderson, B. J., & Rodgers, D. J. (2013). Evidence for water ice near Mercury's north pole from MESSENGER Neutron Spectrometer measurements. *Science*, 339(6117), 292–296.
- Li, S., Lucey, P. G., Milliken, R. E., Hayne, P. O., Fisher, E., Williams, J. P., & Elphic, R. C. (2018). Direct evidence of surface exposed water ice in the lunar polar regions. *Proceedings of the National Academy of Sciences*, 115, 8907–8912.
- Liu, Y., Guan, Y., Zhang, Y., Rossman, G. R., Eiler, J. M., & Taylor, L. A. (2012). Direct measurement of hydroxyl in the lunar regolith and the origin of lunar surface water. *Nature Geoscience*, 5(11), 779.
- Lucey, P., Korotev, R. L., Gillis, J. J., Taylor, L. A., Lawrence, D., Campbell, B. A., & Mendillo, M. (2006). Understanding the lunar surface and space-Moon interactions. *Reviews in Mineralogy and Geochemistry*, 60(1), 83–219.
- Lucey, P. G., Hawke, B. R., Pieters, C. M., Head, J. W., & McCord, T. B. (1986). A compositional study of the Aristarchus region of the Moon using near-infrared reflectance spectroscopy. *Journal of Geophysical Research: Solid Earth*, 91(B4), 344–354.
- Marchi, S., Morbidelli, A., & Cremonese, G. (2005). Flux of meteoroid impacts on Mercury. *Astronomy & Astrophysics*, 431(3), 1123–1127.
- Mazrouei, S., Ghent, R. R., Bottke, W. F., Parker, A. H., & Gernon, T. M. (2019). Earth and Moon impact flux increased at the end of the Paleozoic. *Science*, 363(6424), 253–257.
- McEwen, A. S., & Bierhaus, E. B. (2006). The importance of secondary cratering to age constraints on planetary surfaces. *Annual Review of Earth and Planetary Sciences*, 34, 535–567.
- McEwen, A. S., Preblich, B. S., Turtle, E. P., Artemieva, N. A., Golombek, M. P., Hurst, M., & Christensen, P. R. (2005). The rayed crater Zunil and interpretations of small impact craters on Mars. *Icarus*, 176(2), 351–381.
- McKinnon, W. B., & Parmentier, E. M. (1986). Ganymede and Callisto. In *Satellites (A87-23307 09-91)* (pp. 718–763). Tucson, AZ: University of Arizona Press.
- Melosh, H. J. (1985). Ejection of rock fragments from planetary bodies. *Geology*, 13(2), 144–148.
- Melosh, H. J. (1989). Impact cratering: A geologic process, *Research supported by NASA* (Vol. 253, pp. 11). New York: Oxford University Press (Oxford Monographs on Geology and Geophysics, No. 11).
- Michikami, T., Hagermann, A., Morota, T., Haruyama, J., & Hasegawa, S. (2017). Oblique impact cratering experiments in brittle targets: Implications for elliptical craters on the Moon. *Planetary and Space Science*, 135, 27–36.
- Miller, R. S. (2012). Statistics for orbital neutron spectroscopy of the Moon and other airless planetary bodies. *Journal of Geophysical Research*, 117, E00H19. <https://doi.org/10.1029/2011JE003984>

- Milliken, R. E., & Li, S. (2017). Remote detection of widespread indigenous water in lunar pyroclastic deposits. *Nature Geoscience*, *10*(8), 561.
- Minton, D. A., Fassett, C. I., Hirabayashi, M., Howl, B. A., & Richardson, J. E. (2019). The equilibrium size-frequency distribution of small craters reveals the effects of distal ejecta on lunar landscape morphology. *Icarus*, *326*, 63–87.
- Molaro, J., & Byrne, S. (2012). Rates of temperature change of airless landscapes and implications for thermal stress weathering. *Journal of Geophysical Research*, *117*, E10011. <https://doi.org/10.1029/2012JE004138>
- Molaro, J. L., Byrne, S., & Langer, S. A. (2015). Grain scale thermoelastic stresses and spatiotemporal temperature gradients on airless bodies, implications for rock breakdown. *Journal of Geophysical Research: Planets*, *120*, 255–277. <https://doi.org/10.1002/2014JE004729>
- Molaro, J. L., Byrne, S., & Le, J. L. (2017). Thermally induced stresses in boulders on airless body surfaces, and implications for rock breakdown. *Icarus*, *294*, 247–261.
- Morris, R. V. (1978). In situ reworking/gardening of the lunar surface—Evidence from the Apollo cores. *In Lunar and Planetary Science Conference Proceedings*, *9*, 1801–1811.
- Morris, R. V., Lauer, H. V. Jr., & Gose, W. A. (1979). Characterization and depositional and evolutionary history of the Apollo 17 deep drill core. *Proceedings Lunar Planetary Science Conference 10th*, *2*, 1141–1157.
- Moses, J. I., Rawlins, K., Zahnle, K., & Dones, L. (1999). External sources of water for Mercury's putative ice deposits. *Icarus*, *137*(2), 197–221.
- Nakamura, Y., Dorman, J., Duennebieber, F., Lammlein, D., & Latham, G. (1975). Shallow lunar structure determined from the passive seismic experiment. *The Moon*, *13*(1-3), 57–66.
- Needham, D. H., & Kring, D. A. (2017). Lunar volcanism produced a transient atmosphere around the ancient Moon. *Earth and Planetary Science Letters*, *478*, 175–178.
- Neish, C. D., Blewett, D. T., Harmon, J. K., Coman, E. I., Cahill, J. T. S., & Ernst, C. M. (2013). A comparison of rayed craters on the Moon and Mercury. *Journal of Geophysical Research: Planets*, *118*, 2261. <https://doi.org/10.1002/jgre.20166>
- Neish, C. D., Bussey, D. B. J., Spudis, P., Marshall, W., Thomson, B. J., Patterson, G. W., & Carter, L. M. (2011). The nature of lunar volatiles as revealed by Mini RF observations of the LCROSS impact site. *Journal of Geophysical Research*, *116*, E01005. <https://doi.org/10.1029/2010JE003647>
- Neukum, G. (1983). *Meteoritenbombardement Und Datierung Planetarer Oberflachen*. Munich, Germany: Habilitation Dissertation for Faculty Membership, Ludwig-Maximilians-Univ.
- Neukum, G., Ivanov, B. A., & Hartmann, W. K. (2001). Cratering records in the inner solar system in relation to the lunar reference system. *In Chronology and evolution of Mars* (pp. 55–86). Dordrecht: Springer.
- Neumann, G. A., Cavanaugh, J. F., Sun, X., Mazarico, E. M., Smith, D. E., Zuber, M. T., et al. (2013). Bright and dark polar deposits on Mercury: Evidence for surface volatiles. *Science*, *339*, 296–300. <https://doi.org/10.1126/science.1229764>
- Nishiizumi, K., Welten, K. C., & Caffee, M. W. (2019). Recent deposition and mixing history of the Apollo 17 drill core 70009-70001. 50th Lunar and Planetary Science Conference, held 18-22 March, 2019 at The Woodlands, Texas. LPI Contribution No. 2132, id.2277
- Nozette, S., Spudis, P. D., Robinson, M. S., Bussey, D. B. J., Lichtenberg, C., & Bonner, R. (2001). Integration of lunar polar remote sensing data sets: Evidence for ice at the lunar south pole. *Journal of Geophysical Research*, *106*(E10), 23,253–23,266.
- Oberbeck, V. R., Quaide, W. L., Mahan, M., & Paulson, J. (1973). Monte Carlo calculations of lunar regolith thickness distributions. *Icarus*, *19*(1), 87–107.
- Ong, L., Asphaug, E. I., Korycansky, D., & Coker, R. F. (2010). Volatile retention from cometary impacts on the Moon. *Icarus*, *207*(2), 578–589.
- Paige, D. A., Siegler, M. A., Harmon, J. K., Neumann, G. A., Mazarico, E. M., Smith, D. E., & Solomon, S. C. (2013). Thermal stability of volatiles in the north polar region of Mercury. *Science*, *18*, 3000–303.
- Pierazzo, E., & Melosh, H. J. (2000). Melt production in oblique impacts. *Icarus*, *145*(1), 252–261. <https://doi.org/10.1006/icar.1999.6332>
- Prem, P., Artemieva, N. A., Goldstein, D. B., Varghese, P. L., & Trafton, L. M. (2015). Transport of water in a transient impact-generated lunar atmosphere. *Icarus*, *255*, 148–158.
- Prieur, N. C., Rolf, T., Luther, R., Wünnemann, K., Xiao, Z., & Werner, S. C. (2017). The effect of target properties on transient crater scaling for simple craters. *Journal of Geophysical Research: Planets*, *122*, 1704–1726. <https://doi.org/10.1002/2017JE005283>
- Quaide, W., & Oberbeck, V. (1975). Development of the mare regolith: Some model considerations. *The Moon*, *13*(1-3), 27–55.
- Rubanenko, L., Mazarico, E., Neumann, G. A., & Paige, D. A. (2018). Ice in micro cold traps on Mercury: Implications for age and origin. *Journal of Geophysical Research: Planets*, *123*, 2178–2191. <https://doi.org/10.1029/2018JE005644>
- Rubanenko, L., Venkatraman, J., & Paige, D. A. (2019). Thick ice deposits in shallow simple craters on the Moon and Mercury. *Nature Geoscience*, *12*(8), 597–601.
- Shoemaker, E. M. (1965). The Nature of the Lunar Surface: Proceedings of the 1965 IAU-NASA symposium held at Goddard Space Flight Center, April 15–16, 1965. Sponsored by IAU Commission 17 (the Moon) and NASA. Edited by Wilmot N. Hess, Donald H. Menz and John A. O'Keefe. Library of Congress Catalog Card Number 65-27671; QB591.C748 1965 c.2. Published by the Johns Hopkins Press, Baltimore, MD USA, 1965, p.23.
- Siegler, M. A., Miller, R. S., Keane, J. T., Laneuville, M., Paige, D. A., Matsuyama, I., & Poston, M. J. (2016). Lunar true polar wander inferred from polar hydrogen. *Nature*, *531*(7595), 480.
- Slade, M. A., Butler, B. J., & Muhleman, D. O. (1992). Mercury radar imaging: Evidence for polar ice. *Science*, *258*(5082), 635–641.
- Speyerer, E. J., Povilaitis, R. Z., Robinson, M. S., Thomas, P. C., & Wagner, R. V. (2016). Quantifying crater production and regolith overturn on the Moon with temporal imaging. *Nature*, *538*(7624), 215–218.
- Spudis, P. D., Bussey, D. B. J., Baloga, S. M., Cahill, J. T. S., Glaze, L. S., Patterson, G. W., & Ustinov, E. A. (2013). Evidence for water ice on the Moon: Results for anomalous polar craters from the LRO Mini RF imaging radar. *Journal of Geophysical Research: Planets*, *118*, 2016–2029. <https://doi.org/10.1002/jgre.20156>
- Stacy, N. J. S., Campbell, D. B., & Ford, P. G. (1997). Arecibo radar mapping of the lunar poles: A search for ice deposits. *Science*, *276*(5318), 1527–1530.
- Stewart, B. D., Pierazzo, E., Goldstein, D. B., Varghese, P. L., & Trafton, L. M. (2011). Simulations of a comet impact on the Moon and associated ice deposition in polar cold traps. *Icarus*, *215*(1), 1–16. <https://doi.org/10.1016/j.icarus.2011.03.014>
- Susorney, H. C., James, P. B., Johnson, C. L., Chabot, N. L., Ernst, C. M., Mazarico, E. M., & Kinczyk, M. J. (2019). The thickness of radar-bright deposits in Mercury's northern hemisphere from individual Mercury Laser Altimeter tracks. *Icarus*, *323*, 40–45.
- Syal, M. B., Schultz, P. H., & Riner, M. A. (2015). Darkening of Mercury's surface by cometary carbon. *Nature Geoscience*, *8*(5), 352.
- Thomson, B. J., Bussey, D. B. J., Neish, C. D., Cahill, J. T. S., Heggy, E., Kirk, R. L., & Ustinov, E. A. (2012). An upper limit for ice in Shackleton crater as revealed by LRO Mini RF orbital radar. *Geophysical Research Letters*, *39*, L14201. <https://doi.org/10.1029/2012GL052119>
- Turtle, E. P., & Pierazzo, E. (2001). Thickness of a European ice shell from impact crater simulations. *Science*, *294*(5545), 1326–1328.

- Urey, H. C. (1952). *The planets: Their origin and development*. New Haven, CT: Yale University Press.
- Vasavada, A. R., Paige, D. A., & Wood, S. E. (1999). Near-surface temperatures on Mercury and the Moon and the stability of polar ice deposits. *Icarus*, *141*(2), 179–193.
- Vickery, A. M. (1986). Size-velocity distribution of large ejecta fragments. *Icarus*, *67*(2), 224–236.
- Watson, K., Murray, B. C., & Brown, H. (1962). The stability of volatiles in the solar system. *Icarus*, *1*(1-6), 317–327.
- Williams, J.-P., Bandfield, J. L., Paige, D. A., Powell, T. M., Greenhagen, B. T., Taylor, S., et al. (2018). Lunar cold spots and crater production on the moon. *Journal of Geophysical Research: Planets*, *123*(9), 2380–2392.
- Williams, J. P., Pathare, A. V., & Aharonson, O. (2014). The production of small primary craters on Mars and the Moon. *Icarus*, *235*, 23–36.
- Yasui, M., Schulson, E. M., & Renshaw, C. E. (2017). Experimental studies on mechanical properties and ductile to brittle transition of ice silica mixtures: Young's modulus, compressive strength, and fracture toughness. *Journal of Geophysical Research: Solid Earth*, *122*, 6014–6030. <https://doi.org/10.1002/2017JB014029>
- Zuber, M. T., Head, J. W., Smith, D. E., Neumann, G. A., Mazarico, E., Torrence, M. H., & Melosh, H. J. (2012). Constraints on the volatile distribution within Shackleton crater at the lunar south pole. *Nature*, *486*(7403), 378.